Distribution Category:
High-Level Radioactive Waste
Disposal in Tuff
(UC-814)

ANL-96/16

ARGONNE NATIONAL LABORATORY
9700 South Cass Avenue
Argonne, Illinois 60439

ANALYSIS OF COMPONENTS FROM DRIP TESTS WITH ATM-10 GLASS

by

J. A. Fortner, J. K. Bates, and T. J. Gerding

Chemical Technology Division

September 1996

DISCLAIMER

TABLE OF CONTENTS

LIST OF FIGURES

LIST OF FIGURES (contd.)

LIST OF FIGURES (contd.)

LIST OF TABLES

ANALYSIS OF COMPONENTS FROM DRIP TESTS WITH ATM-10 GLASS

by

Jeffrey A. Fortner, John K. Bates, and Thomas J. Gerding

ABSTRACT

Waste package assemblies consisting of actinide-doped West Valley ATM-10 reference glass and sensitized 304L stainless steel have been reacted with simulated repository groundwater using the Unsaturated Test Method. Analyses of surface corrosion and reaction products resulting from tests that were terminated at scheduled intervals between 13 and 52 weeks are reported. Analyses reveal complex interactions between the groundwater, the sensitized stainless steel waste form holder, and the glass. Alteration phases form that consist mainly of smectite clay, brockite, and an amorphous thorium iron titanium silicate, the latter two incorporating thorium, uranium, and possibly transuranics. The results from the terminated tests, combined with data from tests that are still ongoing, will help determine the suitability of glass waste forms in the proposed high-level repository at the Yucca Mountain Site.

I. INTRODUCTION AND BACKGROUND

Samples of reacted ATM-10 glass (an approved test material that was designated as an initial West Valley Reference glass) and sensitized 304L type stainless steel (ss), generated as part of the N3 series Unsaturated Test (drip tests) [1] sponsored by the Yucca Mountain Project (YMP), have been maintained in storage since 1987 and 1988. These samples, together with the solution results from the tests [2,3], provide a valuable indication of the reaction of ATM-10 glass in the unsaturated environment that may exist at the proposed high-level waste repository site at Yucca Mountain, Nevada. These data are the only long-term durability test results regarding the behavior of a radioactive West Valley glass.

Tests with the Unsaturated Test Method [1] were initiated with the actinide-doped West Valley reference glass ATM-10 [4] on July 6, 1987. The testing of the glass has been supported by the YMP. The tests have followed the original matrix shown in the Task Plan (Table 1) and during the first 52 weeks, eight tests were terminated. In addition to the test samples generated (glass and 304L ss), solutions were collected and analyzed. However, the test samples were not previously analyzed, and solution results were only recently made available [2,3]. As part of the High Level Waste Technical Support Program supported by the Environ-mental Waste Management branch of DOE (EM-324), this Task allows for a combination of the solution and solids analyses to give an overall description of the long-term behavior of a West Valley glass under simulated repository conditions.

Table 1. N3 Test Matrix

Test No.	Description	Date Started	Date Terminated	Cumulative Test Period (weeks)
N3#1	Batch	7/6/87	10/1/87	12.5
N3#2	Batch	7/6/87	10/1/87	12.5
N3#3	Batch	7/6/87	1/4/88	26
N3#4	Batch	7/6/87	1/4/88	26
N3#5	Batch	7/6/87	4/4/88	39
N3#6	Batch	7/6/87	4/4/88	39
N3#7	Batch	7/6/87	7/4/88	52
N3#8	Batch	7/6/87	7/4/88	52
N3#9[a]	Continuous	7/6/87	Ongoing	>450
N3#10[a]	Continuous	7/6/87	Ongoing	>450
N3#11[a,b]	Continuous-blank	7/6/87	Ongoing	>450
N3#12[a]	Continuous	10/6/87	Ongoing	>450

[a]N3#9 through N3#12 remain ongoing under YMP guidance.

[b]N3#11 is a blank test, that is, it contains no glass waste form or holder.

A. Objective

The objective of the N3 Components Task is to analyze the solid components from the N3 Test, by using a combination of techniques to evaluate the process by which the glass reacts, the interaction between the glass and the 304L ss that makes up part of the test assembly, and the distribution of radionuclides between the glass and the steel. These results, when combined with the published solution data, are important input for the glass source term for evaluation of repository performance.

Analyses performed have included optical microscopy, scanning electron microscopy (SEM), and analytical transmission electron microscopy (AEM) techniques. These microscopic techniques allow determination of size and distribution of reaction products and corrosion damage, plus elemental analyses by energy dispersive X-ray fluorescence spectroscopy (EDS) and electron energy loss spectroscopy (EELS) and, in selected cases, crystal structure determination by electron diffraction (ED). Quality Assurance Procedures governing the performance of the analyses used in this task are given in Table 2.

Other tests were performed on the 304L ss components to assess its interaction with the glass waste form. Inductively-coupled plasma/ mass spectroscopy (ICP-MS) was performed on acid-wash from solutions from the stainless steel components to measure transuranic sorption onto the steel on the acid-wash solutions and to also measure boron, silicon, thorium, and uranium deposition onto the metal. Oxalic acid treatment was used to determine the level of sensitization of the 304L ss used in the components.

Table 2. Operating Procedures Governing Analysis of N3 Test Components

Procedure Identification Number (date of issuance)	Procedure Title
NNWSI-05-029	Comparative Quantitative Analysis of Glasses Using SEM/EDS/WDS
NNWSI-05-021	Procedure for Qualitative Description of Test Components
DP-005-068 (2/4/93)	Procedure for Lattice Imaging Using the Transmission Electron Microscope
DP-005-069 (2/4/93)	Procedure for Electron Diffraction Using the Transmission Electron Microscope
DP-005-070 (3/9/93)	Procedure for X-Ray Energy Dispersive Spectra (EDS) Acquisition and Analysis Using the Transmission Electron Microscope
DP-005-086 (3/9/93)	Procedure for Sample Tracking and Data Reporting for TEM Samples

II. TECHNICAL APPROACH

The Unsaturated Test, or drip test, has been completed on the N3 batch samples according to standard procedure [1]. The test matrix is shown in Table 1. Tests N3#9 through N3#12 remain ongoing under YMP guidance, with solution analyses being performed at each sampling period. Test N3#11 is a blank (control) test, containing no waste form, and is used to monitor groundwater injections into the test vessels and to check for possible cross-contamination of radionuclides between tests. To provide a basis for understanding the data presented in this Report, a brief description of the initial test components and the Unsaturated Test procedure follows.

A. Preparation and Selection of Initial Components

1. Preparation of ATM-10 Glass

The actinide-doped West Valley ATM-10 reference glass was received from the Materials Characterization Center (MCC) at Pacific Northwest National Laboratory. The composition of the glass is given in Table 3 [4]. The ATM-10, like other West Valley glasses, is unusual compared to other U.S. high-level waste glasses because it contains relatively large concentrations of thorium and phosphorous oxides, 3.29 and 2.34 wt %, respectively. The unusual composition of the ATM-10 originates from its unique waste stream at the West Valley Demonstration Project, the only commercial reprocessing facility for civilian nuclear fuel to have operated in the U.S. The ATM-10 glass was received in the form of cast bars. These glass bars were subsequently crushed; the powder was transferred to a platinum crucible and remelted in an 1150°C oven within a helium-filled glovebox. The glass was poured into Pt/Au molds preheated at 770°C and annealed at 500°C for 15 minutes, then allowed to cool in the powered-down oven. The short annealing time was used to impart some stress to the glass while still allowing for sectioning into test components. The cast glass was then cut to size; the final finish on the tops and bottom were as-cut surfaces, while the sides were as-cast. The finished samples of ATM-10 glass consisted of eleven gently tapered cylinders with these approximate dimensions: 16.0 mm in diameter at the top, 15.4 mm in diameter at the bottom, and 20.2 mm in length. Each weighed about 10.5 grams. Variation of each of the above-mentioned dimensional parameters was less than 5%. The glass appeared homogeneous and black. The original ATM-10 glass [4] contained small amounts (less than 2 wt %) of ruthenium oxide and iron chromium spinel phases. These devitrification phases were also noted on subsequent SEM examination of the surfaces of the reacted N3 glass samples. Similar devitrification phases have been observed in other West Valley glasses, WV6 [5] and WV-205 [6], for instance.

2. Sensitization of the 304L Stainless Steel

The ATM-10 glass was held in place for the tests by a waste form holder made of 304L ss that had been perforated with holes to allow free contact with the dripping water (see Fig. 1). Compositional certifications supplied by the manufacturers indicated that the 304L ss wire used to make the support posts contained more than twice the carbon of the perforated plate material (0.037% versus 0.016%). Type 304L ss will be used to fabricate the pour canister for glass waste forms in the repository. The 304L ss components used in the N3 tests were sensitized by annealing for 24 hours in a 550°C oven to simulate the result of pouring molten glass into the canisters during production of actual waste. The final color of the metal was a deep blue. Metallurgical testing of the degree of sensitization was performed, and is discussed in a later section of this Report.

Table 3. Composition of the ATM-10 Glass[a]

Oxide	Mean, wt %	Std. Dev., wt %
Al_2O_3	6.65	0.0209
AmO_2	0.0064	0.000073
B_2O_3	9.17	0.082
BaO	0.045	0.00131
CaO	0.60	0.0354
CeO_2	0.072	0.00127
Cr_2O_3	0.253	0.0107
CsO_2	0.062	0.0015
Fe_2O_3	11.5	0.2065
K_2O	3.34	0.125
La_2O_3	0.025	0.0020
Li_2O	2.88	0.0281
MgO	1.15	0.0296
MnO_2	1.29	0.0219
Na_2O	10.5	0.150
Nd_2O_3	0.168	0.0023
NiO	0.296	0.0135
NpO_2	0.021	0.00041
P_2O_5	2.34	0.258
PuO_2	0.0081	0.000527
RhO_2	0.012	0.0018
RuO_2	0.061	0.0108
SO_3	0.31	0.090
SiO_2	45.8	2.391
SrO	0.025	0.00096
Tc_2O_7	0.0031	0.000083
ThO_2	3.29	0.0336
TiO_2	0.858	0.0245
UO_2	0.527	0.0171
Y_2O_3	0.017	0.00082
ZrO_2	0.247	0.00513
Total	101.5	

[a]From Maupin et al. [4].

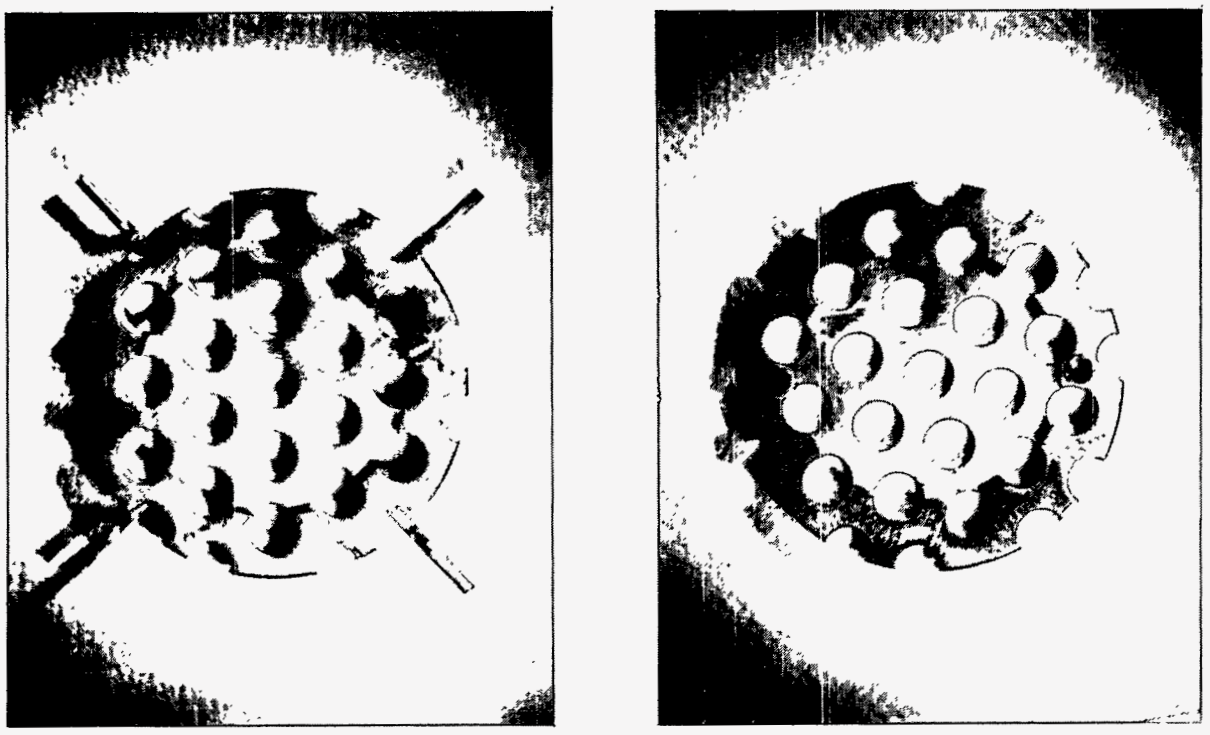

Fig. 1. The 304L ss Retainer Components

B. The Unsaturated Test Method

The Unsaturated Test Method is briefly described here to set the context for the results to be presented. Detailed descriptions are given elsewhere [7-9].

The proposed Yucca Mountain repository site is located in a hydrologically unsaturated zone composed of welded and devitrified tuff. For the first 300-1000 years after interment, the heat generated by radiation will maintain the temperature of the waste package environment above 100°C [10]. During this period, the stainless steel pour canisters are expected to maintain their integrity; thus, liquid water is not expected to make contact with the glass. Later, when the temperature has cooled to below the boiling point of the groundwater and if the canisters have been breached, liquid water and water vapor may contact the waste glass. It is this scenario, where glass, stainless steel, and water (liquid and vapor) interact, that the Unsaturated Test Method was designed to simulate.

In Fig. 2, a schematic diagram of the test vessel and detail of the enclosed waste package assemblage (WPA) are presented. Every 3.5 days, 0.075 mL (equivalent to approximately 3 drops) of EJ-13 water (groundwater from the J-13 well that had been pre-equilibrated at 90°C with local tuff) was injected into the airtight vessel, where it contacted the top surface of the WPA. Each glass monolith is contacted on the top and bottom by the two perforated retainer plates in each holder, which are held in place by two 304L ss wire posts. The entire apparatus was enclosed in a 90°C oven except when samples were taken. (For the terminated tests

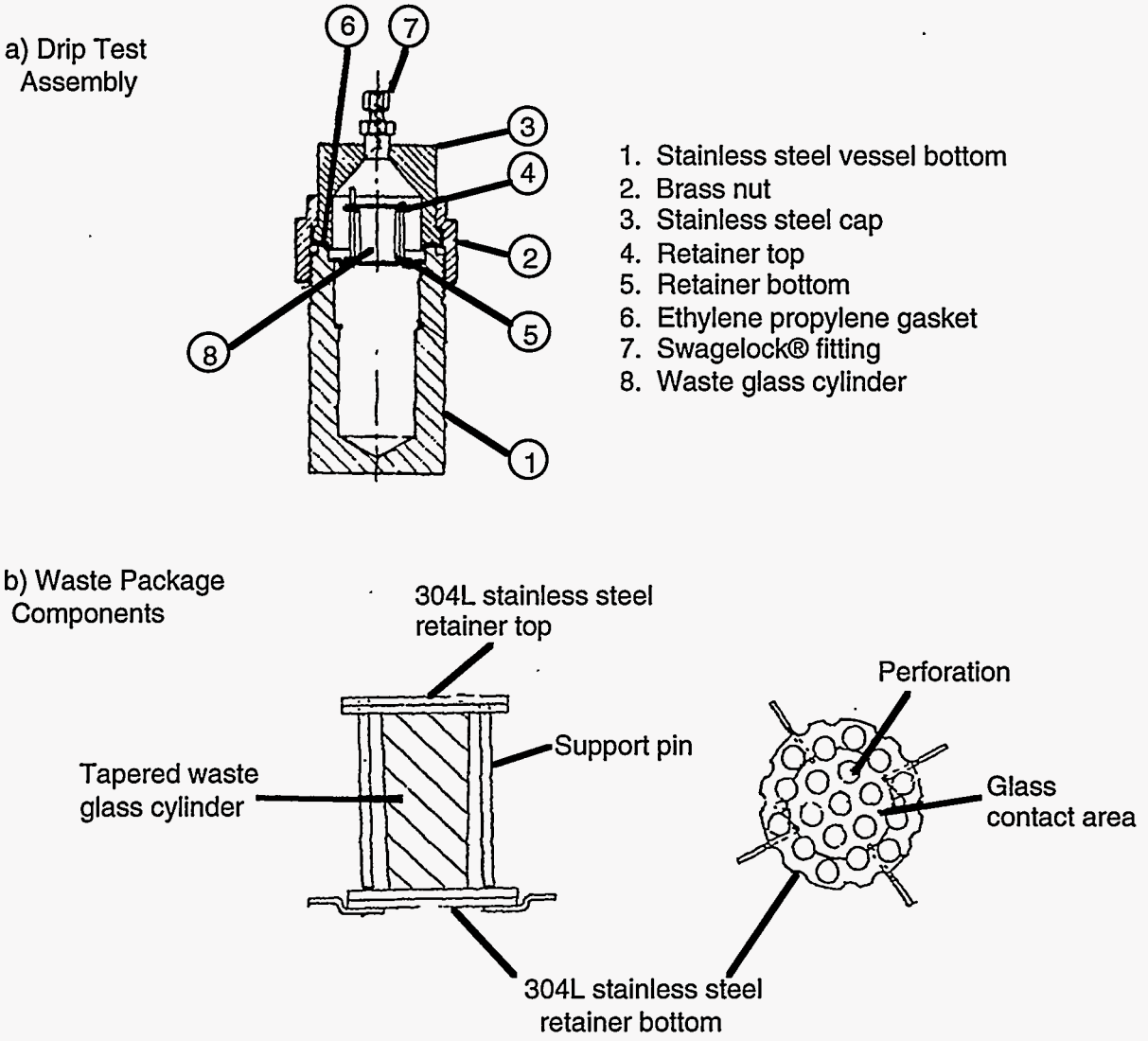

Fig. 2. The Test Vessel Used in the N3 Drip Tests. (a) The containment vessel assembly. (b) The waste package components.

discussed here, samples were taken only once, upon termination). Water dripped down the sides of the glass and accumulated at the bottom of the WPA. Eventually the water dripped from the WPA to the bottom of the vessel; the glass samples were not immersed. The as-analyzed composition of the EJ-13 groundwater is given in Table 4.

Upon termination, the water was collected from the vessel for elemental analysis by inductively coupled plasma-atomic emission spectrometry (ICP-AES) and alpha spectroscopys. These data are reported elsewhere [2,3]. The WPA components were disassembled and weighed, then photographed and stored in labeled containers while awaiting analysis. The mass changes of the glass, the 304L ss retainers, and the total WPA are given in Table 5, and the percent changes are plotted in Fig. 3. The mass changes provide a gross representation of the magnitude of the reaction. The total mass change is small, although it appears that initially mass (in the form of reaction products) is transferred from the glass to the stainless steel. At later times, cations extracted from the EJ-13 water may have reacted with the glass surface or been adsorbed onto it, reversing the initial mass loss of the glass.

Table 4. Composition of the EJ-13 Water[a] Used in the N3 Tests

Species	Concentration (mg/L)[b]
Al	0.7
B	0.2
Ca	6.6
Fe	<0.1
K	7
Mg	0.15
Li	0.04
Na	53
Si	40
F^-	3
Cl^-	10
NO_2^-	<1
NO_3^-	11
SO_4^{2-}	23
HCO_3^-	100
Total Carbon	25
Organic Carbon	7

[a]The pH of EJ-13 water is ~8.6.

[b]Other cations are < 0.1 mg/L.

Table 5. N3 Test Components Masses before and after Testing

Test	Duration (weeks)	Glass Mass In (g)	Glass Mass Out (g)	Glass Mass Loss (μg)	Glass Relative Mass Loss (%)	304L Top Retainer In (g)	304L Top Retainer Out (g)	304L Top Retainer Mass Gain (μg)
N3#1	12.5	10.42933	10.42915	180	0.0017	3.16609	3.16623	140
N3#2	12.5	10.50925	10.50362[a]	5630[a]	0.0536[a]	3.15144	3.15159	150
N3#3	26	10.67526	10.67421	1050	0.0098	3.15589	3.15600	110
N3#4	26	10.46056	10.45984	720	0.0069	3.18516	3.18519	30
N3#5	39	10.65264	10.65126	1380	0.013	3.13676	3.13703	270
N3#6	39	9.83140	9.83060	800	0.0081	3.14192	3.14219	270
N3#7	52	10.72120	10.72037	830	0.0077	3.16627	3.16632	50
N3#8	52	10.40966	10.40914	521	0.0050	3.17504	3.17496	-80

Test	304L Top Retainer Relative Mass Gain (%)	304L Bottom Retainer In (gm)	304L Bottom Retainer Out (gm)	304L Bottom Retainer Mass Gain (μg)	304L Bottom Retainer Relative Mass Gain (%)	Total 304L Retainer Mass Change (%)	Total Test Mass Change (%)
N3#1	0.0044	4.12108	4.12115	70	0.0017	0.0029	0.00017
N3#2	0.0048	4.08577	4.08581	40	0.00098	0.0026	-0.031[a]
N3#3	0.0035	4.10002	4.10013	110	0.0027	0.0030	-0.0046
N3#4	0.00094	4.08635	4.08636	10	0.00025	0.00055	-0.0038
N3#5	0.0086	4.10659	4.10695	360	0.0088	0.0087	-0.0042
N3#6	0.0086	4.11724	4.11752	280	0.0068	0.0076	-0.0015
N3#7	0.0016	4.11610	4.11611	10	0.00024	0.00083	-0.0043
N3#8	-0.0025	4.10819	4.10808	-110	-0.0027	-0.0026	-0.0040

[a]The N3#2 glass monolith was accidentally chipped between testing and reweighing; these masses do not reflect the actual performance of the glass in this particular test.

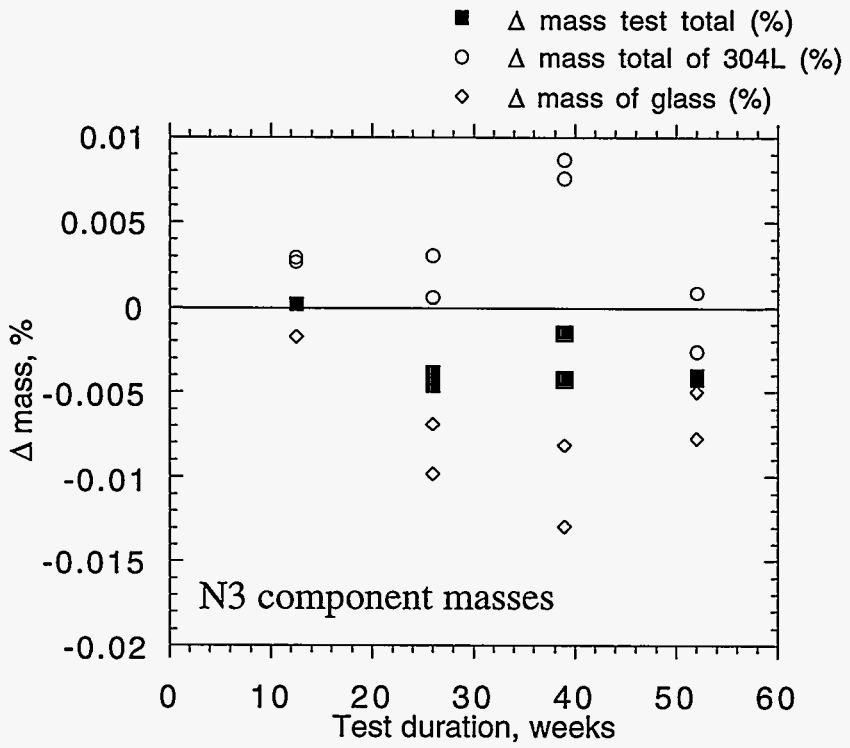

Fig. 3. Percent Mass Changes of the N3 Test Components. One outlier, the N3#2 glass, was accidentally chipped between the initial weighing and the post-test weighing and is not included in the figure.

C. Analytical Techniques

1. Optical Microscopy

All glass samples were visually examined, and their top and bottom surfaces photographed under an optical microscope before any further analyses. All surfaces of the 304L ss retainer plates that had been in contact with the glass were also examined and photographed under an optical microscope.

2. Scanning Electron Microscopy

Whole glass and stainless steel surfaces were examined in an ISI® Super II® scanning electron microscope (SEM) equipped with a PGT® energy dispersive X-ray fluorescence spectroscopy (EDS) system for elemental identification. Images could be formed from either backscattered electrons or secondary electrons, the former providing atomic number (i.e., Z) contrast, the latter providing contour and electrical conductivity contrast. Most SEM micrographs were taken in backscatter mode, as this provided quick indication of alteration phases rich in iron, thorium, and uranium. The as-reacted surfaces were examined normal to the surface, providing a topological scan of the reacted glass and stainless steel. The SEM was also used to examine the sensitization of the 304L ss in cross section after a metallurgical procedure was carried out to reveal grain boundaries. Useful magnifications of up to 5000X could be achieved with this instrument.

3. Analytical Transmission Electron Microscopy

Selected materials were removed from the glass surfaces of N3#1, N3#3, N3#5, and N3#8 for examination wotj analytical transmission electron microscopy (AEM). Materials taken included chips of glass, often with an attached clay reaction layer, and alteration phases from the surface. These samples, measuring between 10 and 100 μm across, were imbedded in an epoxy resin and sectioned with a diamond knife to form ~50- to 100-nm-thick sections with ultramicrotomy. Typically, between five and eight samples were successfully prepared and analyzed from each glass surface. These samples provided cross-sectional images of the surface. Details of the AEM sample preparation technique are presented elsewhere [11].

The sample sections rested on a standard carbon-coated transmission electron microscopy (TEM) grid and were analyzed in a JEOL 2000FXII transmission electron microscope operating at 200 keV. The microscope was equipped with a NORAN® ultrathin window EDS detector, a Gatan® parallel energy loss spectroscopy (EELS) detection system, and a Gatan® slow-scan charge-coupled device (CCD) camera. The microscope was operated either in an image mode, where useful magnifications from 1000X to more than 100,000X were recorded, or in a diffraction mode, which allowed positive identification of several crystalline secondary phases.

III. RESULTS AND DISCUSSION

A. Qualitative Description of Components

1. Optical Examination

Qualitative optical examinations have been completed for all relevant surfaces, both glass and 304L ss, including photographs taken in the optical microscope.

Increased quantities of clay and other alteration phases were observed on the glass and stainless steel components with increasing test duration. Observed changes on the glass surfaces included white-, blue-, or rust-colored discoloration and evidence of particulate growth of alteration phases. Stainless steel surfaces had rusted areas, particularly around perforation holes, and patches of alteration phases. The bottoms of the glass samples were much more frequently observed to display substantial evidence of interaction with the stainless steel retainer than the tops; likewise, the bottom stainless steel retainer displayed more evidence of corrosion than the tops. Figure 4 shows optical micrographs of the N3#1 (12-1/2-week test) through the N3#8 (52-week test) glass surfaces. Note the increased appearance of reaction (as water marks and debris from alteration phases) on the samples progressing from N3#1 to N3#8 and from top surface to bottom surfaces. Note also the large marks on the bottom of the longer-duration tests glasses, which appeared rust-colored. For the tests of shorter duration (i.e., N3#1 and N3#2), the contact areas between the glass and stainless steel often had a light metallic blue appearance. This bluish coloration persisted in the longer-duration tests, surrounding the rust-colored markings.

Optical examination of the stainless steel retainers revealed little material attached to the top components and, generally, little rust. In sharp contrast, the bottom components were covered with increasing amounts (with test duration) of clay and alteration phases. In addition, heavy rust appeared in the area of the retainer posts, which had been TIG welded to the bottom retainer (Fig. 5). The concentration of the rust near the welds is consistent with increased sensitization of the 304L ss in this area. These areas of heavier rust also explained the diametrically opposed rust (or blue) markings on the bottom surfaces of the glass monoliths (see Fig. 4). These findings enable us to examine how sensitization of the stainless steel affects its interaction with the waste glass, as different regions of the same glass surface have been exposed to differently sensitized stainless steel. Again, rust appearance, both near the posts welds and elsewhere on the bottom stainless steel components, increased with test duration.

2. SEM Examination of Glass Surfaces

Scanning electron microscopy (SEM) has been completed for representative surfaces for samples from each completed time duration: N3#1 (13 weeks), N3#3 (26 weeks), N3#5 (39 weeks), and N3#8 (52 weeks).

It is instructive to compare the optical and SEM backscattered electron images of the glass sample surfaces (Figs. 6 and 7). In Fig. 6, the same area of the bottom of the N3#1 monolith is depicted by both techniques. Note how the light patches in the optical image appear as dark (low atomic number) patches in the SEM image. These regions of lower atomic number are an alteration phase having a lower density than the glass. Figure 7 shows a large rust mark on the bottom of N3#8 in both backscatter SEM and optical modes. In this case, the optical

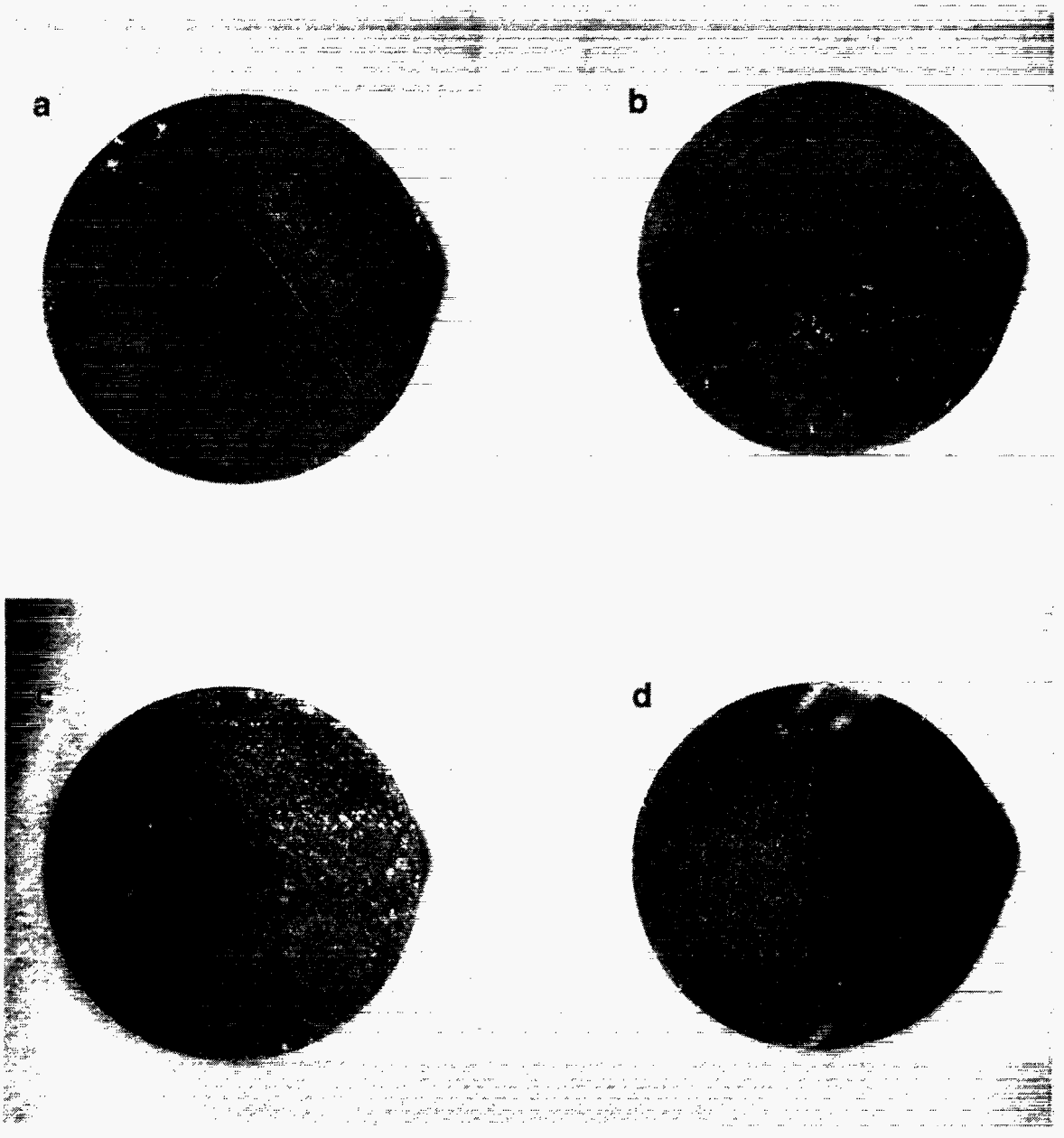

Fig. 4. Optical Images from the Glass Monoliths from the Batch N3 Tests. (a) N3#1 (12-1/2-week test) top; (b) N3#1 bottom; (c) N3#2 (12-1/2-week test) top; (d) N3#2 bottom. The magnification is approximately 4.8X.

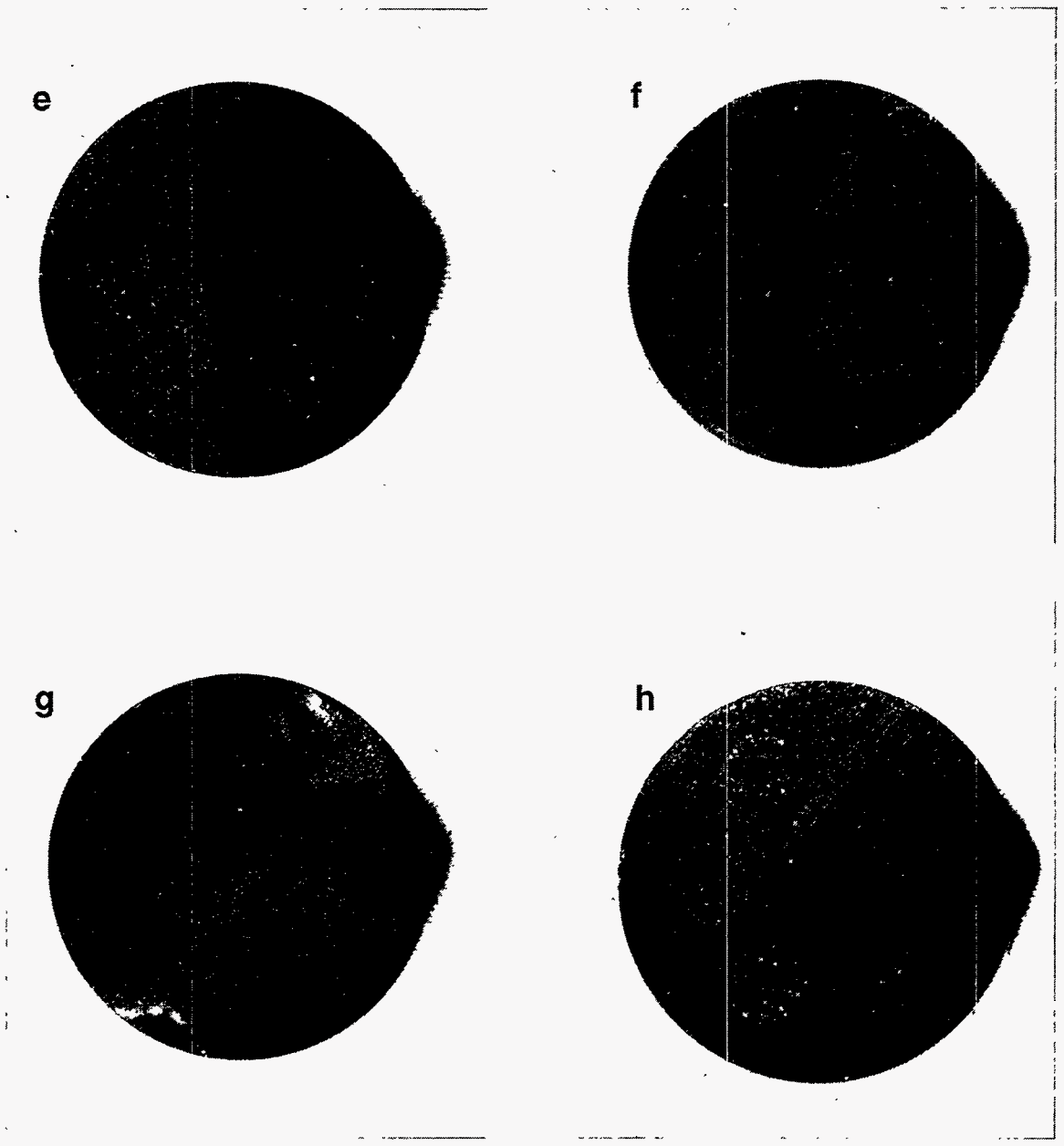

Fig. 4 (contd.) (e) N3#3 (26-week test) top; (f) N3#3 bottom; (g) N3#4 (26 week test) top; (h) N3#4 bottom. The magnification is approximately 4.8X.

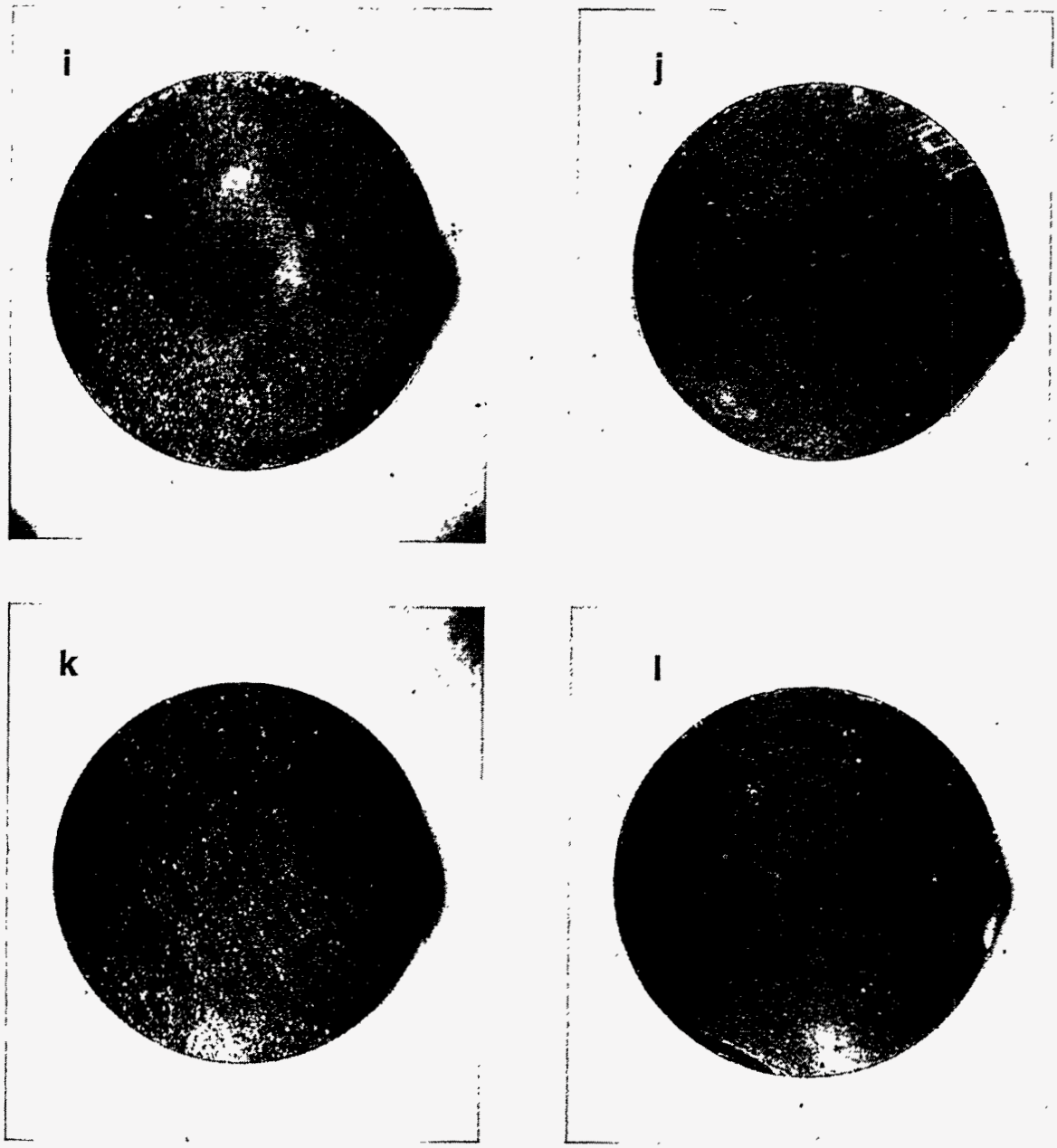

Fig. 4 (contd.) (i) N3#5 (39-week test) top; (j) N3#5 bottom; (k) N3#6 (39-week test) top; (l) N3#6 bottom. The magnification is approximately 4.8X.

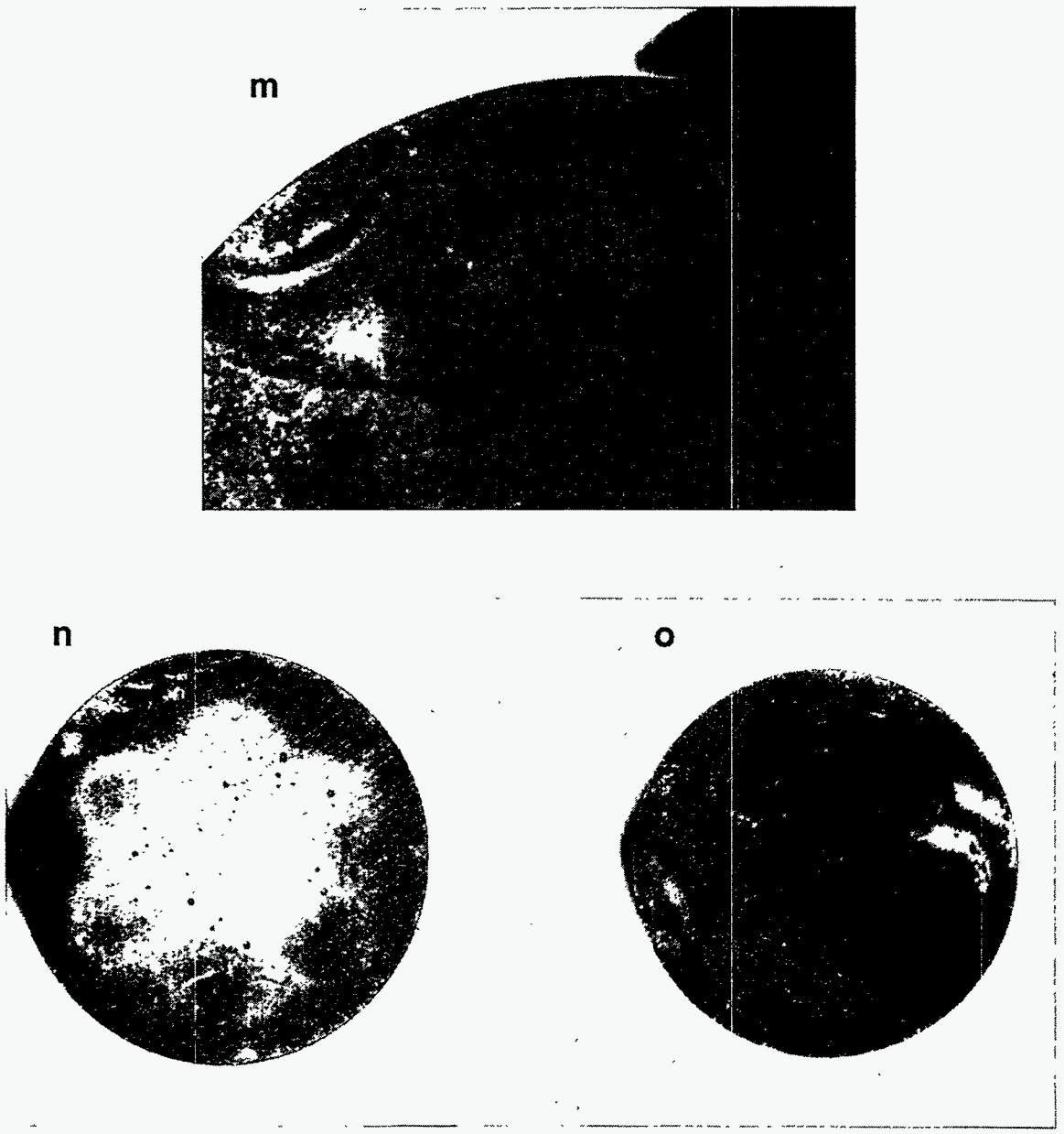

Fig. 4 (contd.) (m) N3#7 (52-week test) bottom, detail. Magnification is approximately 16X (the N3#7 monolith was not cut, and will be kept as an archival sample; its full height precluded its fitting into the low magnification optical microscope); (n) N3#8 (52-week test) top; (o) N3#8 bottom. The magnification is approximately 4.8X.

Fig. 5. Optical Image (detail) of the Bottom 304L ss Sample Retainer near the Welded Post. The post is partially visible as a blur in the upper right-hand corner. The magnification is approximately 25X.

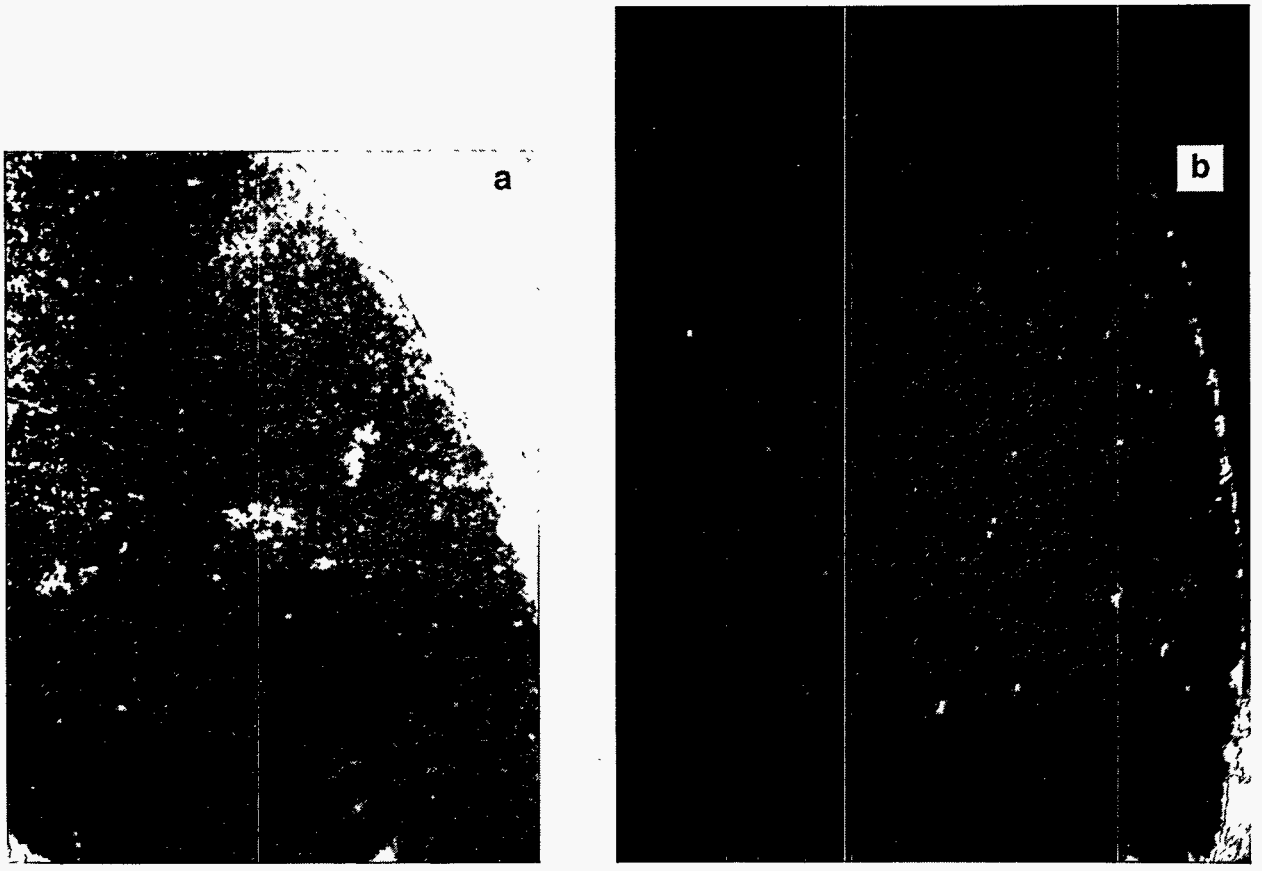

Fig. 6. (a) Optical and (b) Backscattered SEM Images of the Same Area of N3#1 Bottom. The magnification is approximately 15X for both figures.

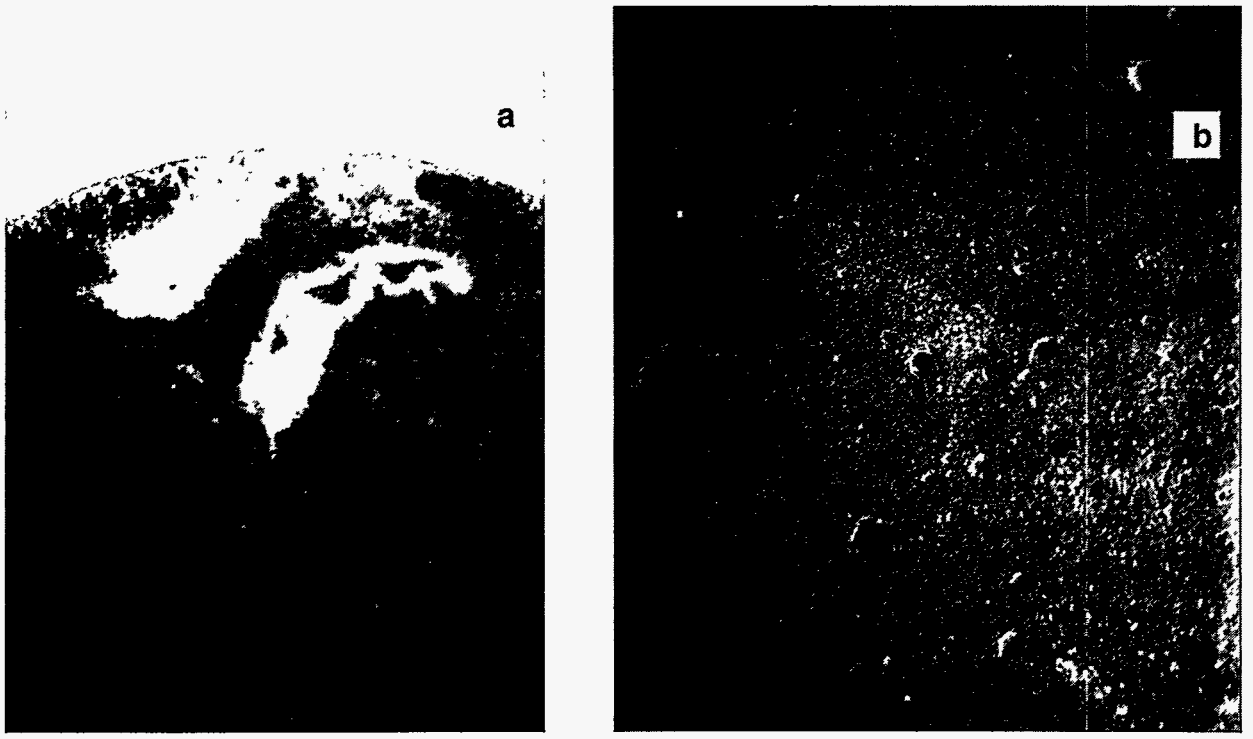

Fig. 7. (a) Optical and (b) Backscattered SEM Images of the Same Area of N3#8 Bottom. The magnification of (a) is approximately 12X, that of (b) is approximately 24X.

image more clearly depicts the evidence of interaction between the glass and stainless steel. The fact that the SEM backscatter images and EDS were not very sensitive to the rust (iron) markings indicates that these layers were generally thin compared to the 20 keV electron-penetration depth into the sample (greater than about 0.5 μm); their thickness was later measured in a TEM to be around 50 nm, as discussed later in this Report (Section III.C.2).

Figure 8 shows a backscattered SEM image of the top surface of the N3#1 glass from an area described as having a blue coloration. The jagged appearance is typical of saw-cut glass, and there is only the slightest suggestion of clay formation and few alteration phases. The bright specks have an iron-chromium composition and are thus attributed to the interaction between the glass and the stainless steel.

Figure 9 is a backscattered SEM micrograph of a region on the bottom of the N3#1 glass monolith, also described as blue. In addition to the tiny iron-chromium particles, a uranium silicate particle measuring ~1 μm across was found. This phase is marked with an arrow on the micrograph. Such uranium silicate phases were not frequently observed on any of the glass surfaces, but they were often associated with the stainless steel. Unfortunately, they were not located in any of the AEM samples. Another uranium silicate particle appears in Fig. 10, a backscattered SEM micrograph from the bottom surface of the N3#3 stainless steel retainer. Although the uranium silicate examples in Figs. 9 and 10 were not widely observed in these drip tests, it should be noted that uranium (VI) silicate particles identified as weeksite ($K_2[UO_2]_2[Si_2O_5]_3 \cdot 4H_2O$) were observed in vapor hydration tests at 200°C of the more recent West Valley reference glass, WV6 [5]. Although the vapor hydration test is extremely aggressive, it generally leads to the formation of the same phases that are observed in long-term MCC-1 tests. This observation suggests that weeksite is a possible, albeit minor, alteration product of the N3 tests.

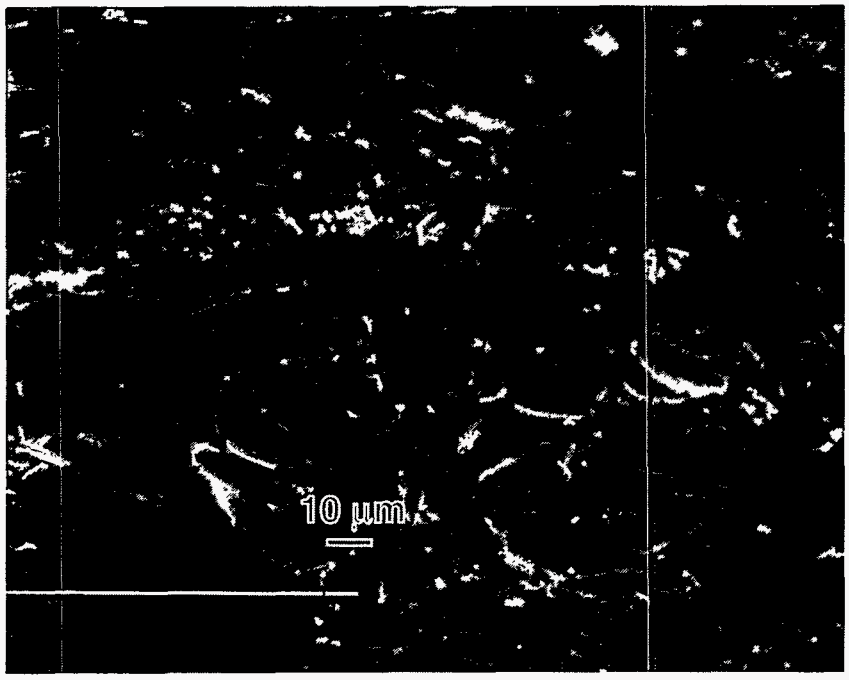

Fig. 8. Backscattered SEM Micrograph of Clay Layer on Glass from the Top Surface of N3#1. The bright specs, corresponding to higher electron density, are iron- and chromium-rich.

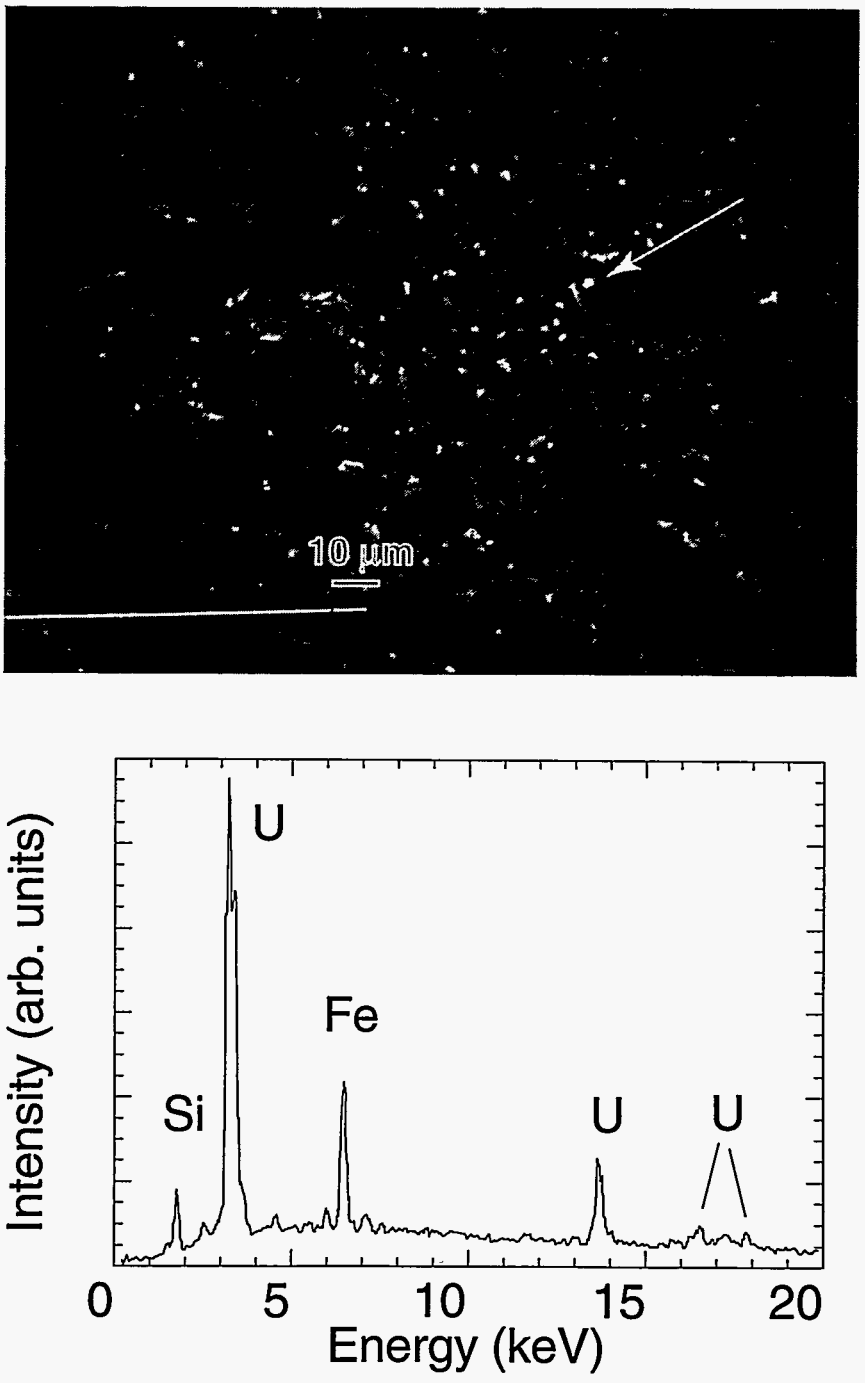

Fig. 9. Backscattered SEM Micrograph of Where the Clay Layer on Glass from the Bottom Surface of N3#1 Interacted with the 304L ss Retainer. Most of the tiny particles have an iron-chromium composition; a single uranium silicate particle, with the EDS spectrum shown below, is identified with the arrow.

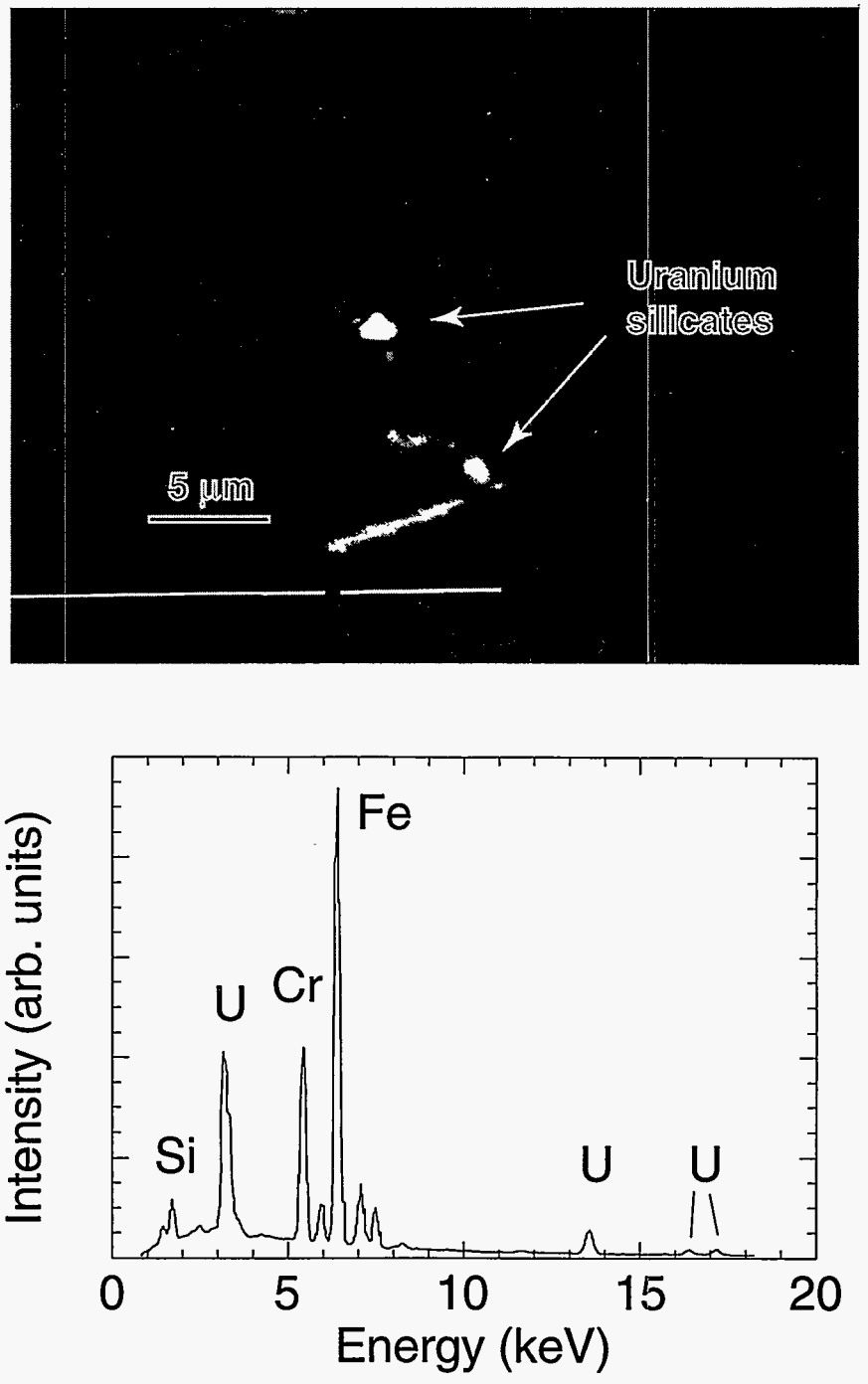

Fig. 10. Backscattered SEM Micrograph of a Uranium Silicate Particle from the Bottom Surface of the 304L ss Retainer in the N3#3 Test and Its EDS Spectrum (below)

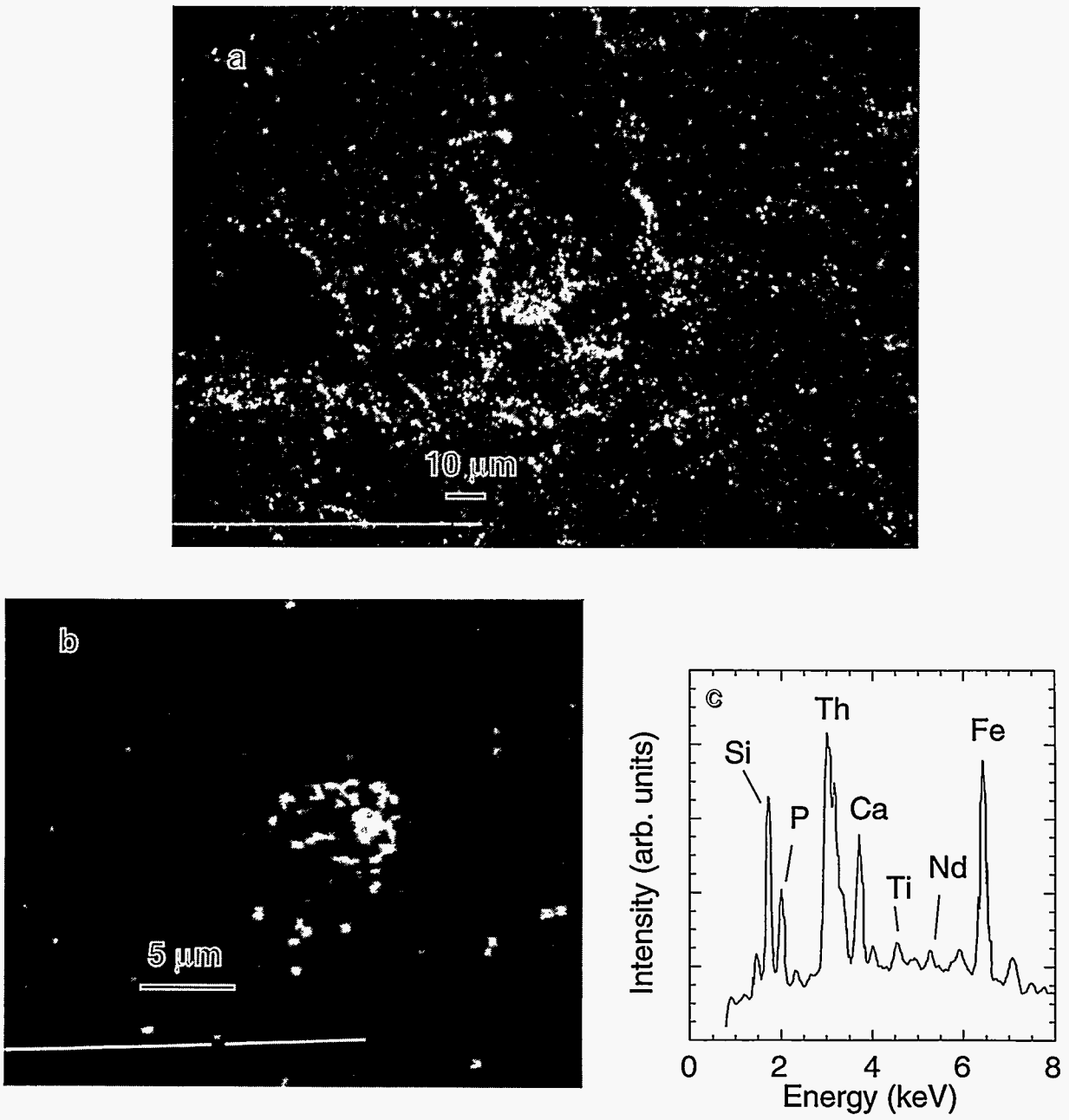

Fig. 11. (a) Backscattered SEM Micrograph of Clay Layer on Glass from the Top Surface of N3#8 Showing Copious Amounts of Brockite Particles (bright speckles). (b) Higher Magnification Detail of a Cluster of Brockite Particles from the Same Region. (c) EDS Spectrum of Brockite Particles.

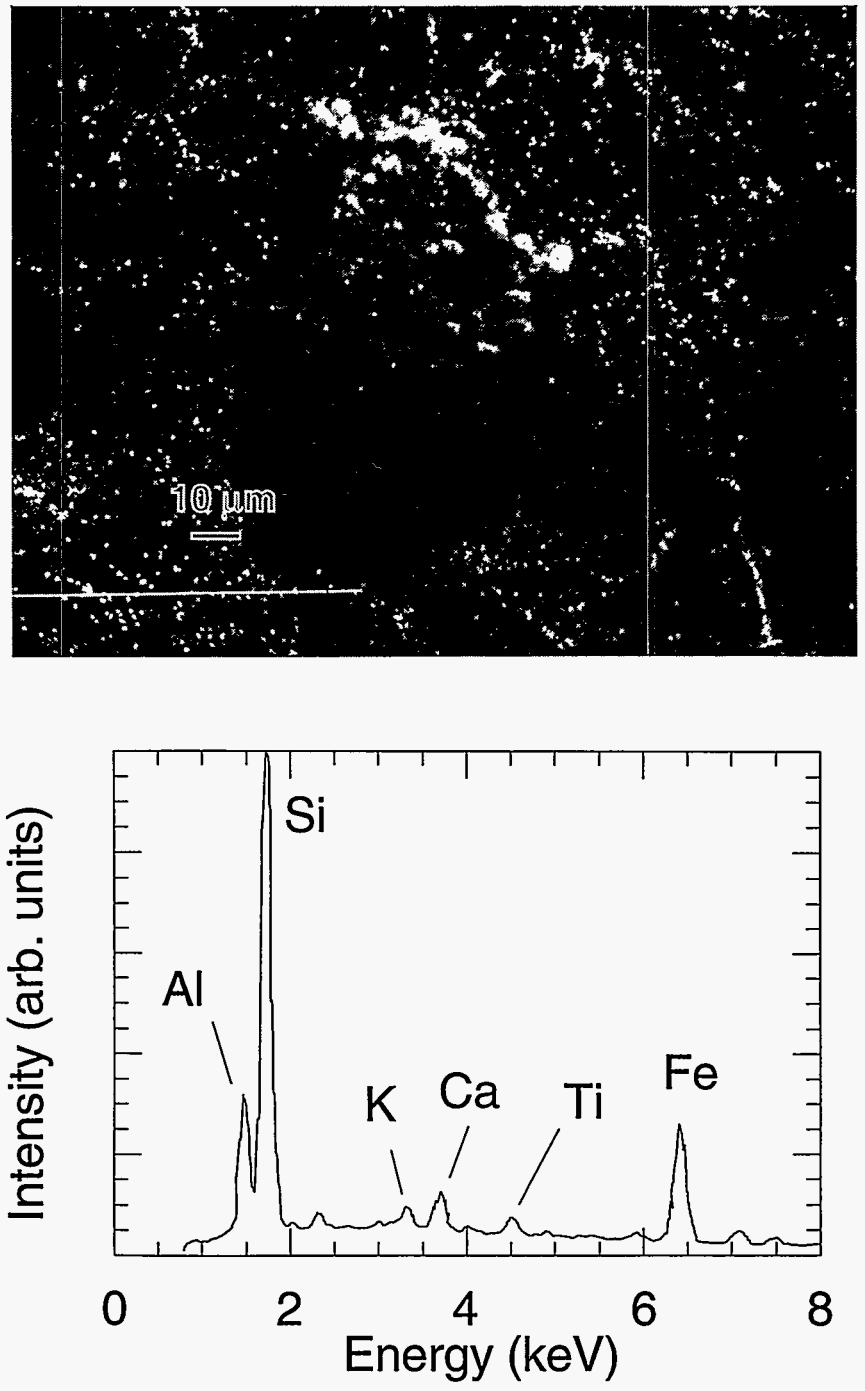

Fig. 12. Backscattered SEM Image of a Potassium-Calcium Aluminosilicate Particle (above) from the Top Surface of N3#8 and Its EDS Spectrum (below).

After longer reaction times (52 weeks), the N3#8 monolith displayed far more evidence of reaction and secondary phase formation. Figure 11a shows a micrograph of the N3#8 top surface, where copious amounts of thorium calcium rare earth phosphate microcrystals had settled. They were identified with electron diffraction (ED) in AEM samples as brockite, $(Ca,La,Th)PO_4$, and these appear as the bright specks in the micrograph. A cluster of these particles is shown in Fig. 11b, revealing their size to be less than 0.5 μm across. From a nearby area, a large particle of potassium-calcium-aluminosilicate (possibly a zeolite, based on its composition) is shown in Fig. 12. The bright specks surrounding and even appearing on the potassium-calcium-aluminosilicate are brockite. As in the case of the uranium silicate phase, potential zeolite phases were rarely encountered. In only one case was a zeolite found among the AEM samples; it was identified with ED to be a member of the hollandite subgroup (see Section III.C.2).

On the bottom of N3#8, more brockite was found including the very large (~5 μm) particle shown in Fig. 13. Iron-rich clay and particles having an iron-silicon composition (Fig. 14) were also observed. These phases were studied in great detail with AEM.

The reaction progress of the glass observed in the SEM begins with the formation of a thin clay layer; the thickness, determined with AEM examination of cross sections, is discussed later in this report. As the clay grows, so do the number and size of discrete thorium-bearing phases. The iron-bearing phases are observed on all glass surfaces and are generally small in size. Infrequently observed phases included uranium silicates and a calcium silicate.

3. SEM Examination of 304L Stainless Steel Components

The stainless steel retainer components of the WPA also displayed increasing amounts of alteration phases on their surfaces with increased test duration. These alteration phases again included clay, brockite, iron oxide, iron silicates, and occasional uranium silicates. The top portion of the stainless steel holder generally had very little of the alteration phase on it, while the bottom often was quite well covered. Table 5 indicates that the top and bottom portions of the stainless steel retainers gained about the same relative mass during each test. Thus, most of this mass gain must be attributed to oxidation, since the much larger population of other alteration phases on the bottom retainer would not be expected from the mass change alone.

Iron oxide and iron silicate particles were commonly seen in great quantity around the welds of the retainer posts of the 304L ss retainer bottoms, regardless of test duration. These particles indicate rapid oxidation of the posts themselves, which contained more carbon within the 304L ss and were subject to greater sensitization by the heat of welding than the perforated retainer plates. The effect of welding on 304L ss is worth noting because the pour canisters used in production will have a welded construction. Figure 15 shows the extent of reaction observed by SEM to have occurred on the bottom stainless steel retainer from N3#3 around a perforation near a retainer post. Figure 16 shows how the alteration phases accumulated on the bottom 304L ss retainer around the perimeter of the glass in N3#8; the retainer post is visible in the lower corner of Fig. 16a, while in Fig. 16b the edge of where the glass had rested on the stainless steel is clearly visible by the sudden change in the density of alteration phases. The role of liquid water in transporting these phases is apparent because the larger density of alteration phases occurs just beyond where the glass was contacting the metal. Figure 17 shows another area from the N3#8 bottom retainer where clay and brockite had accumulated near a different perforation. Figure 18 shows an unusually dense population of brockite microparticles on the top stainless steel retainer; their presence here indicates that they either nucleated *in situ* or floated up from

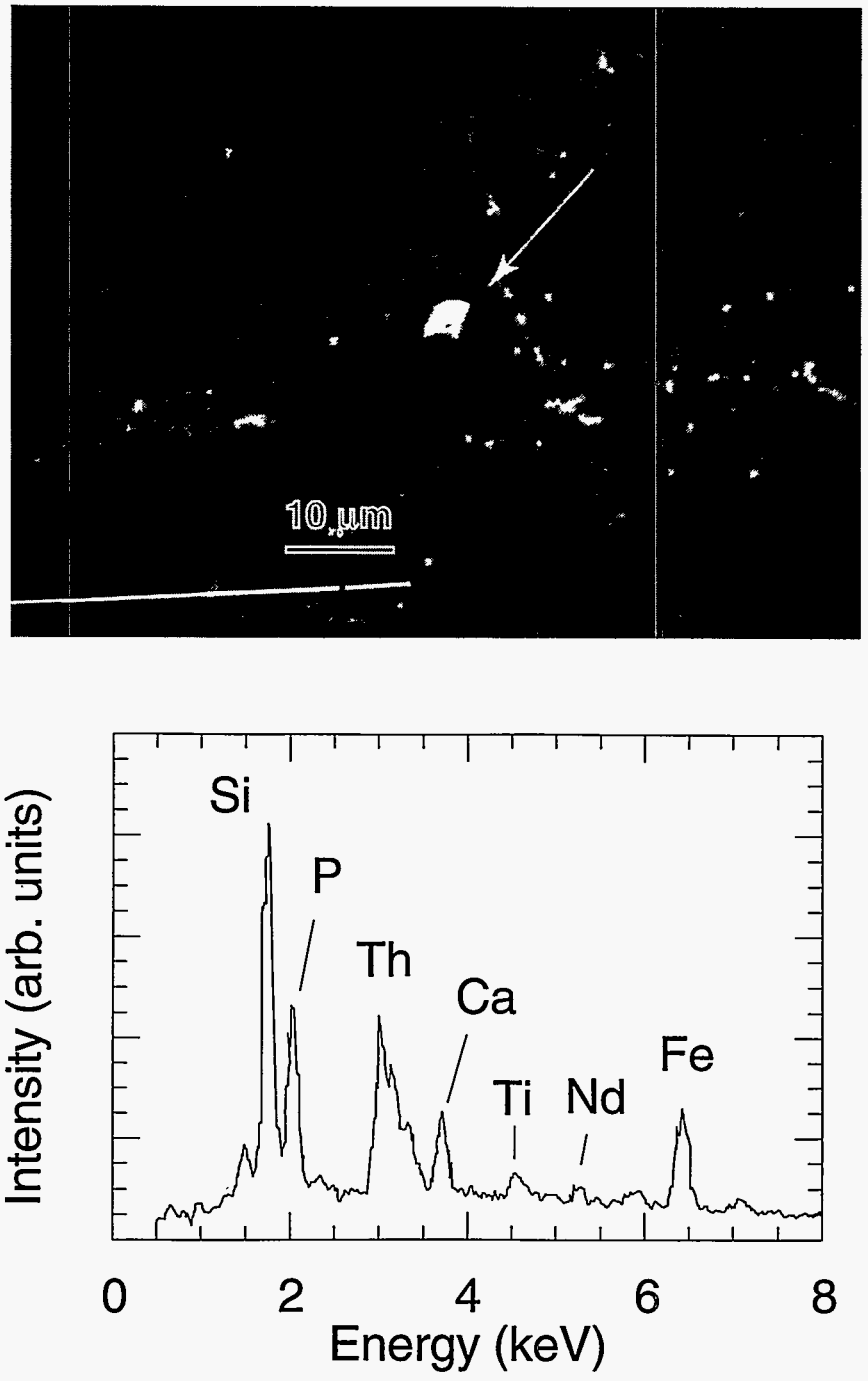

Fig. 13. Backscattered SEM Image of a Large (nearly 5 μm across) Particle of Brockite (above) on the Bottom Surface of the N3#8 Glass and Its EDS Spectrum (below)

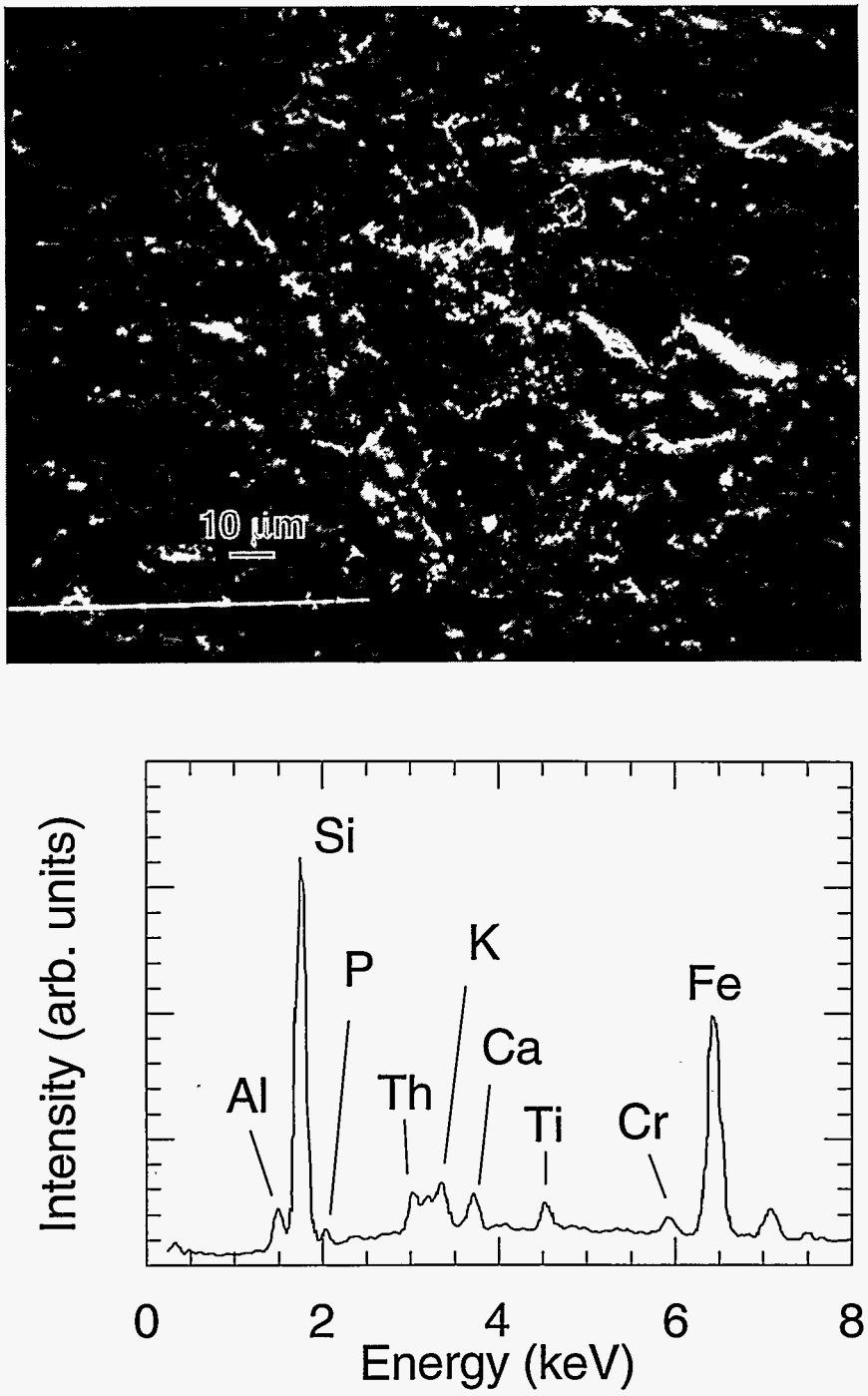

Fig. 14. Backscattered SEM Image of Iron-Rich Clay (above) on the Bottom Surface of the N3#8 Glass and Its EDS Spectrum (below)

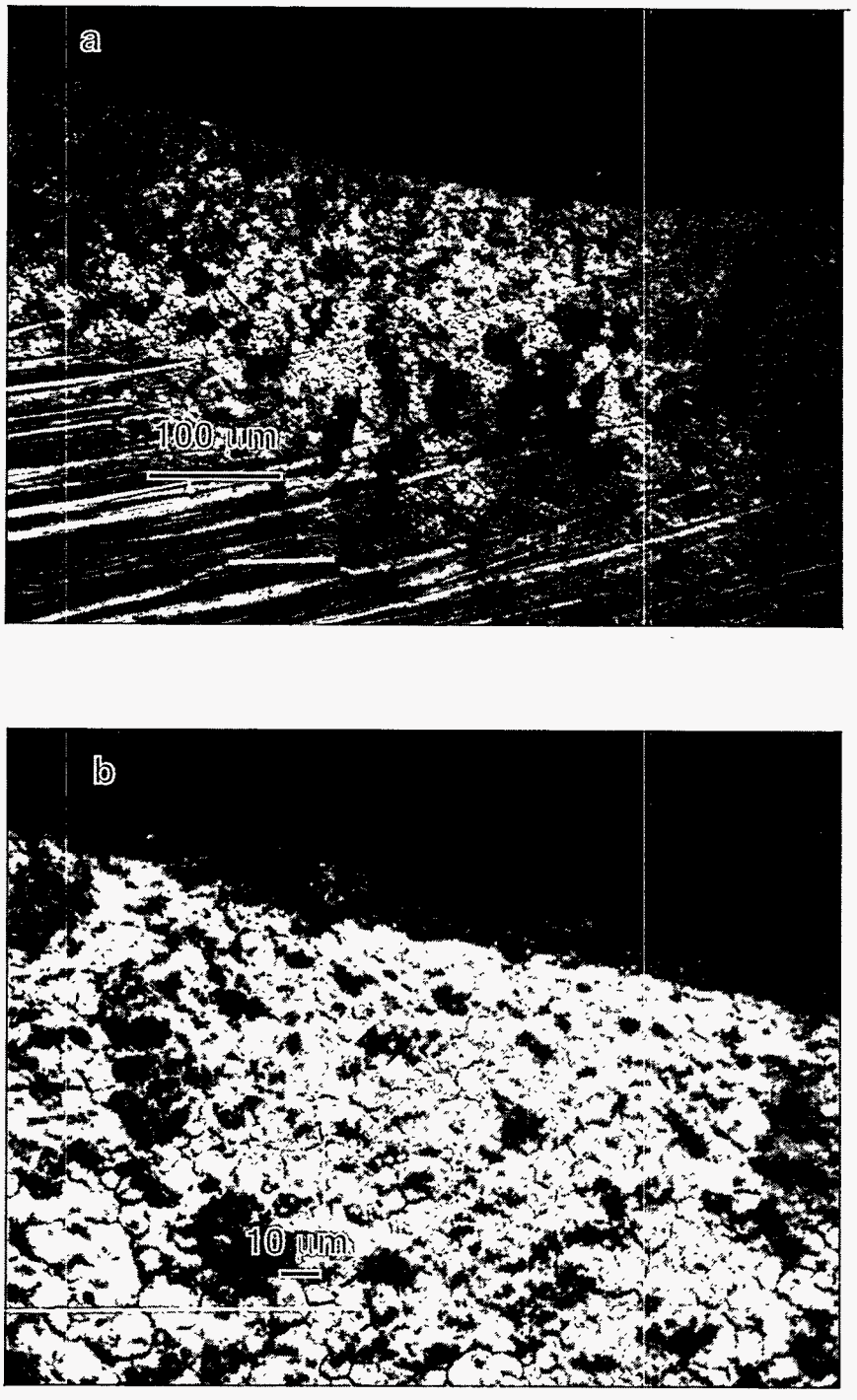

Fig. 15. (a) Backscattered SEM Image of Clay Accumulation on Bottom 304L ss Retainer Components from N3#3, with (b) Higher Magnification Image

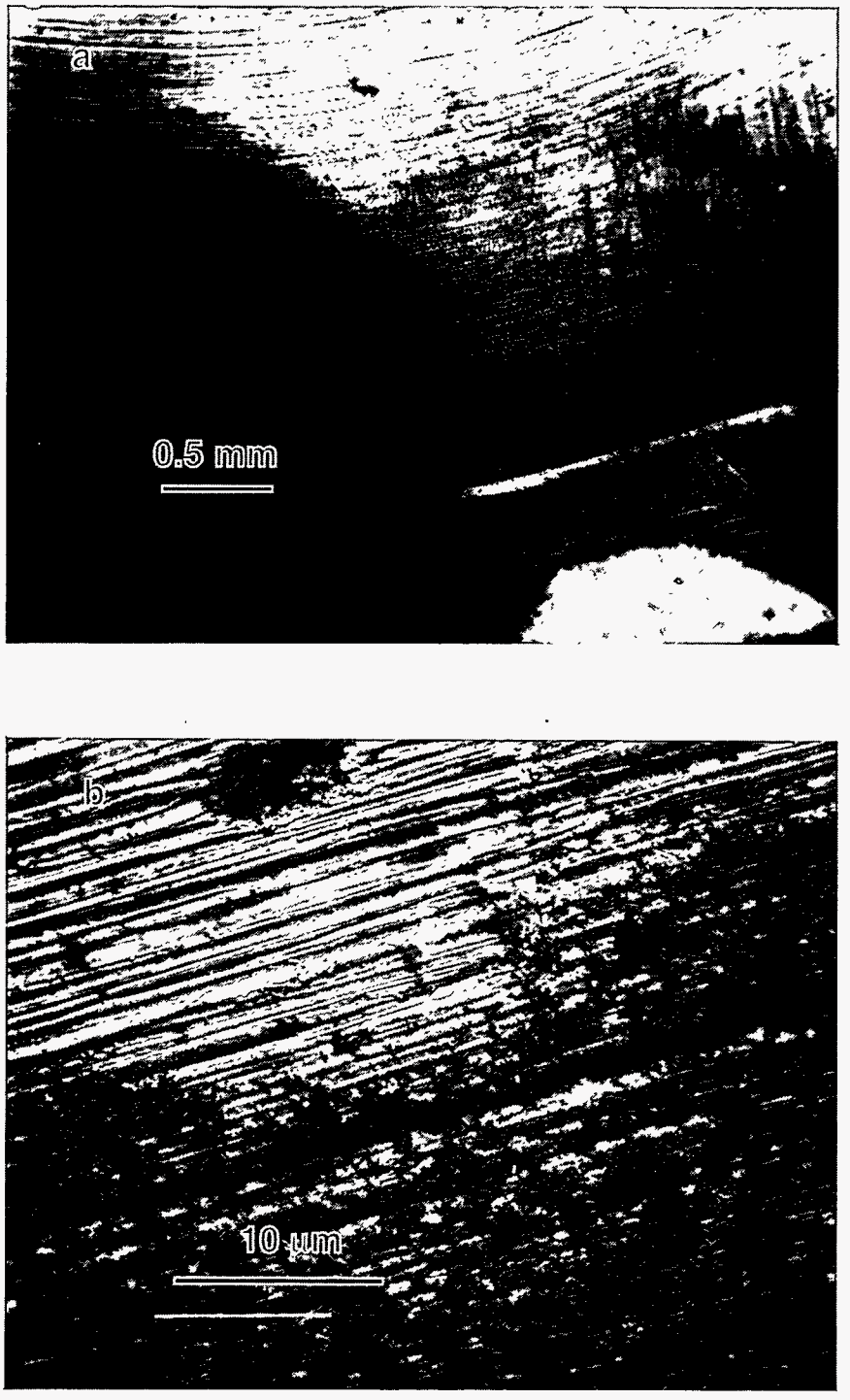

Fig. 16. Backscattered SEM Images of Clay Accumulation on Bottom 304L ss Retainer Components from N3#8. (a) The retainer post is visible in lower corner. (b) The changes in density of the alteration phase indicate where the glass contacted the stainless steel.

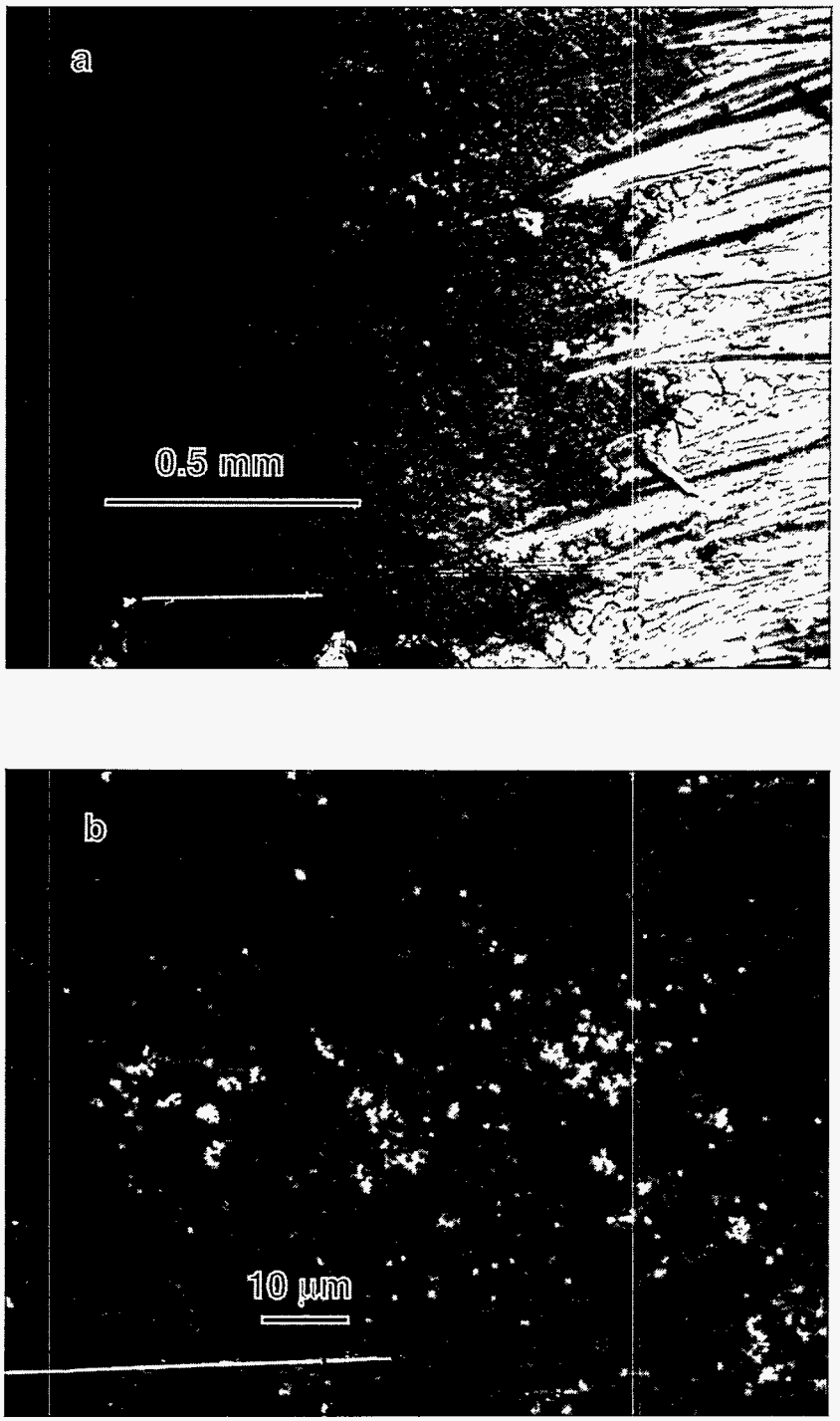

Fig. 17. (a) Backscattered SEM Image of Clay Accumulation (a) on Bottom 304L ss Retainer Components from N3#8. (b) Higher Magnification Image of Clay where Brockite Particles (visible as tiny bright specks) were also Found. (c) EDS Spectrum of Clay, and (d) EDS Spectrum of Brockite in Clay.

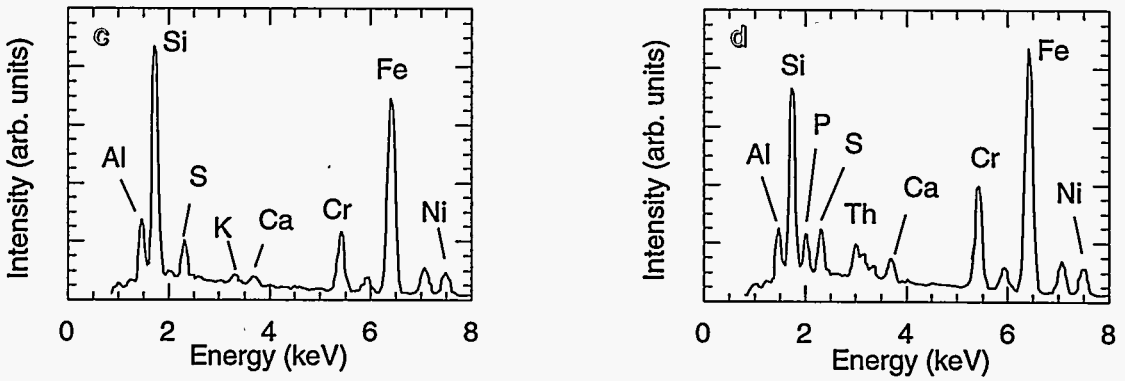
c
Si
Fe
Al
S
K
Ca
Cr
Ni
Intensity (arb. units)
0
2
4
6
8
Energy (keV)
d
Si
Fe
P
Al
S
Cr
Th
Ca
Ni
Intensity (arb. units)
0
2
4
6
8
Energy (keV)

Fig. 17, contd.

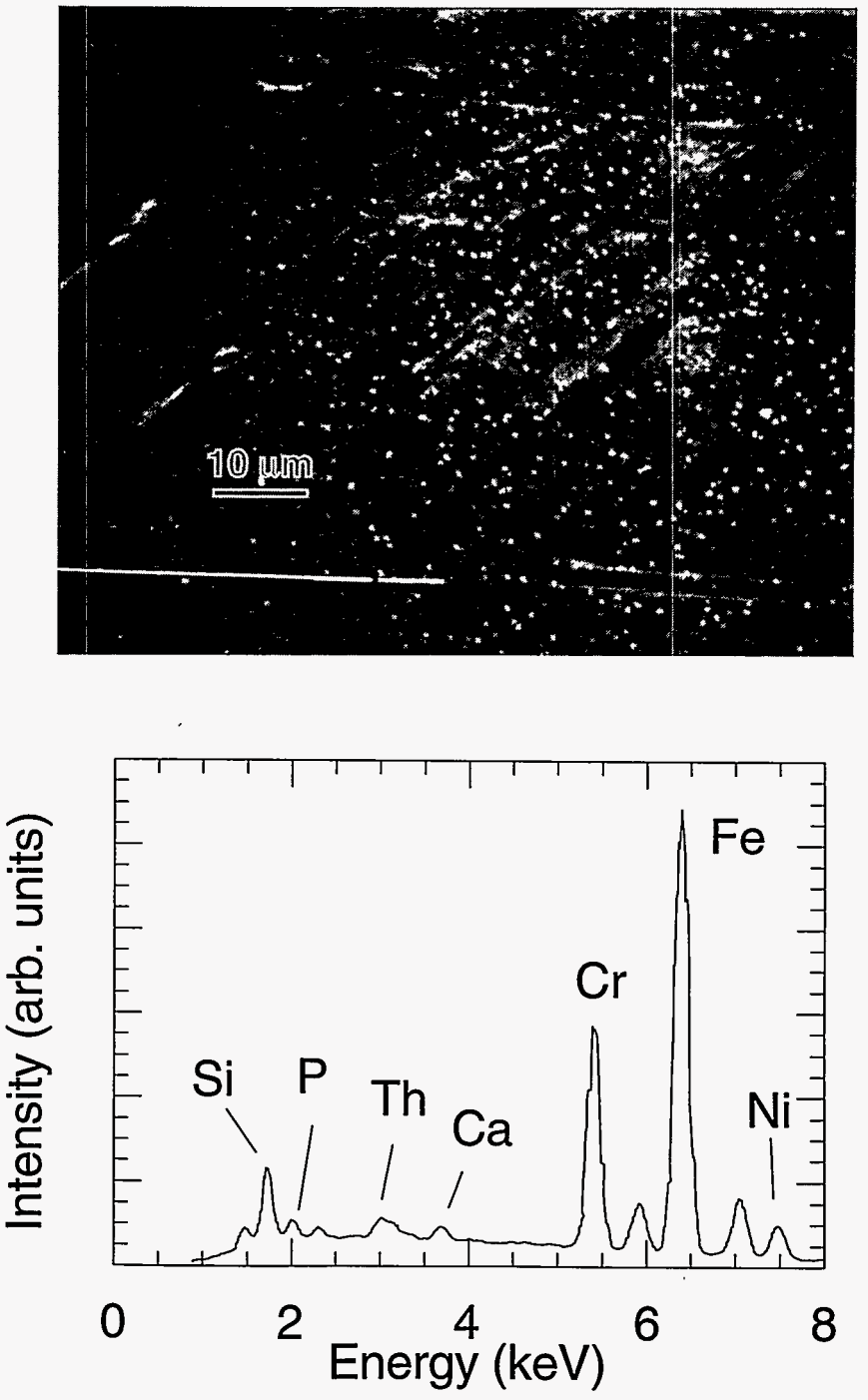

Fig. 18. Backscattered SEM Image of Brockite Particles on the Top 304L ss Retainer Components from N3#8 and Their EDS Spectrum

the glass surface via water that bridged the gap between the glass top and the retainer. These brockite particles are not accompanied by a substantial amount of clay. A summary of the alteration phases observed on the N3 Test components, both glass and 304L ss, through one year of reaction appears in Table 6.

4. 304L Stainless Steel Sensitization

As a test of the role of sensitization of the 304L ss retainer components, one of them (from the N3#2 test) was examined by use of a standard metallurgical procedure [12]. Since all of the retainers were machined from the same 304L ss stock and received the identical heat treatment, we shall consider this N3#2 a representative sample. All of the retainers were noted to have similar appearance (bluish coloration, et cetera) before and after the execution of the tests. Prior to the metallurgical sensitization test, the metal was acid stripped to remove actinides and other alteration products from its exposed surfaces (Section III.B). The metallurgical sensitization test involved preparing a cross section of the metal retainer, imbedding the cross-sectioned sample in epoxy, polishing to a 1 μm diamond finish, then etching with oxalic acid in an electrolytic cell using the sample as the cathode. The etching reveals grain boundary precipitation of chromium carbide, typically caused by heat treatment. The metal is considered to be sensitized only if the grain boundary precipitations form uninterrupted channels. The resultant surfaces are shown in the SEM micrographs of Fig. 19. The interior of the perforated plates comprising the bulk of the retainer assembly shown in Fig. 19a were found to be not sensitized (the etched boundaries do not quite connect continuously). The wire support posts were not sensitized in the interior (Fig. 19b), but were highly sensitized within about 20 μm of the surface (Fig. 19c). Extensive sensitization was also noted in regions of the plates that had been machined (Fig. 19d). Overall, it appears that the desired partial sensitization of the stainless steel retainer components was achieved. The areas most sensitized were clearly responsible for the observed rust marks on the glass and iron alteration phases described above. The sensitized stainless steel reacts more rapidly with water, providing a source of iron that, in turn, will interact with the waste glass and/or with the solution constituents.

B. Elements Retained on the Stainless Steel Waste Package Components

The release of elements to solution from a drip test effectively defines the source term at a point in time. In order to describe the observed solution behavior in terms of the corrosion of the WPA, it is necessary to determine how elements are released from the glass, including those that are retained on thestainless steel retainer either as sorbed species or reacted alteration phases. To this end, thestainless steel retainer components of representative tests at each time interval were stripped with a mixture of hydrofluoric and nitric acids to remove all surface materials. The resultant solutions were submitted for inductively coupled plasma/mass spectroscopy (ICP/MS) analysis to determine actinide and lithium concentrations.

Lithium release is an important benchmark for glass corrosion: it is not present in the stainless steel, it is not a major component of the EJ-13 water, and it is not expected to be substantially incorporated into alteration phases. Thus, little lithium should be found on the stainless steel as it is highly soluble and would be washed away by dripping water, whereas the actinides are expected to sorb onto the metal surfaces.

In Fig. 20, the masses of transuranic elements released to the leachate solution and retained on the stainless steel retainer are compared. The leachate solution data (from the original YMP files) were obtained in 1988 by high resolution alpha spectroscopy. These data are the sum of transuranics in the solution collected upon test termination plus the transuranics dissolved during a nitric acid strip of the test vessel [3] and represent all of the material considered to have left the WPA. The acid strip of the retainer components represents the transuranic material considered to have been sorbed or otherwise fixed on thestainless steel

Table 6. Summary of Alteration Phases Noted on the N3 Surfaces

Phase	Location	Identification	Comments
Smectite clays	A layer on all glass surfaces. Spalled fragments located sporadically on 304L retainer components	EDS, electron diffraction, lattice imaging	A ubiquitous layer that grew in thickness with test duration. The more advanced growths displayed a backbone structure.
Brockite (ideally $CaThPO_4$)	Copious amounts found on most glass surfaces. Clusters found on most 304L retainer surfaces except those of shortest test duration.	EDS, electron diffraction, EELS	Appeared to form as separate crystallites in or on outer layer of clay. Entrained rare earth elements, uranium, and probably transuranics. This phase was amorphous or partly amorphized.
Uranium silicates	Very sparsely located on glass and 304L retainer surfaces. Were possibly more likely to be observed where 304L retainer interacted with glass.	EDS	Positive phase identification of these rarely-encountered crystallites was not possible; they did not appear in any AEM samples.
Iron silicates, iron silicate hydrates, and iron oxyhydrates	In some cases, iron-rich layers grew on glass where it contacted 304L retainer. Separate material and crystals found on most glass and 304L retainer surfaces.	EDS, electron diffraction	Electron diffraction generally found these materials to be amorphous. Fayalite was identified in one instance by electron diffraction.
Thorium titanium iron silicate	Appeared to precipitate colloidally between glass and clay layer or in other regions of restricted water flow.	EDS, EELS	This material was amorphous and grew as wisps that were usually mixed with the clay. The clay appeared to serve as a barrier, trapping this material between the glass and the clay backbone
Zeolites	Rarely encountered (possibly artifacts).	EDS, electron diffraction	Only two instances observed; once in the SEM (N3#8 glass top) and once in the AEM (N3#3 glass bottom). Electron diffraction identified the latter as a member of the heulandite subgroup.
Amorphous silica	Occasional white particulates on most surfaces.	EDS, EELS, electron diffraction (as diffuse rings)	Precipitates on clay surface.

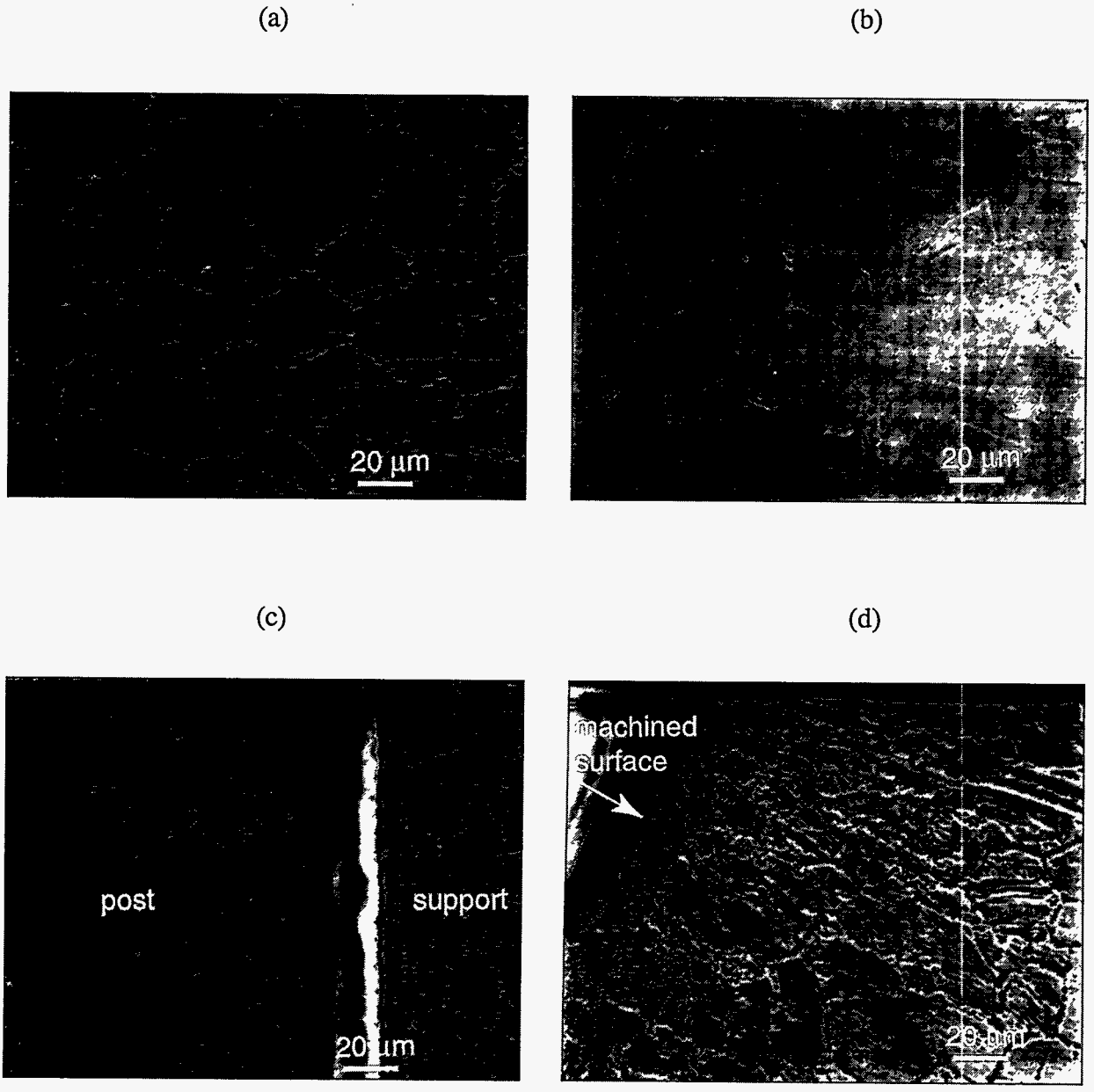

Fig. 19. Sensitization of the 304L ss Retainer Components. The retainer plates were partially sensitized (a), as determined by the etching of the grain boundaries. The wire posts were not sensitized in their interior (b), but were heavily sensitized at the surface (c). Extensive sensitization also occurred near machined portions of the plates, as near a perforation (d).

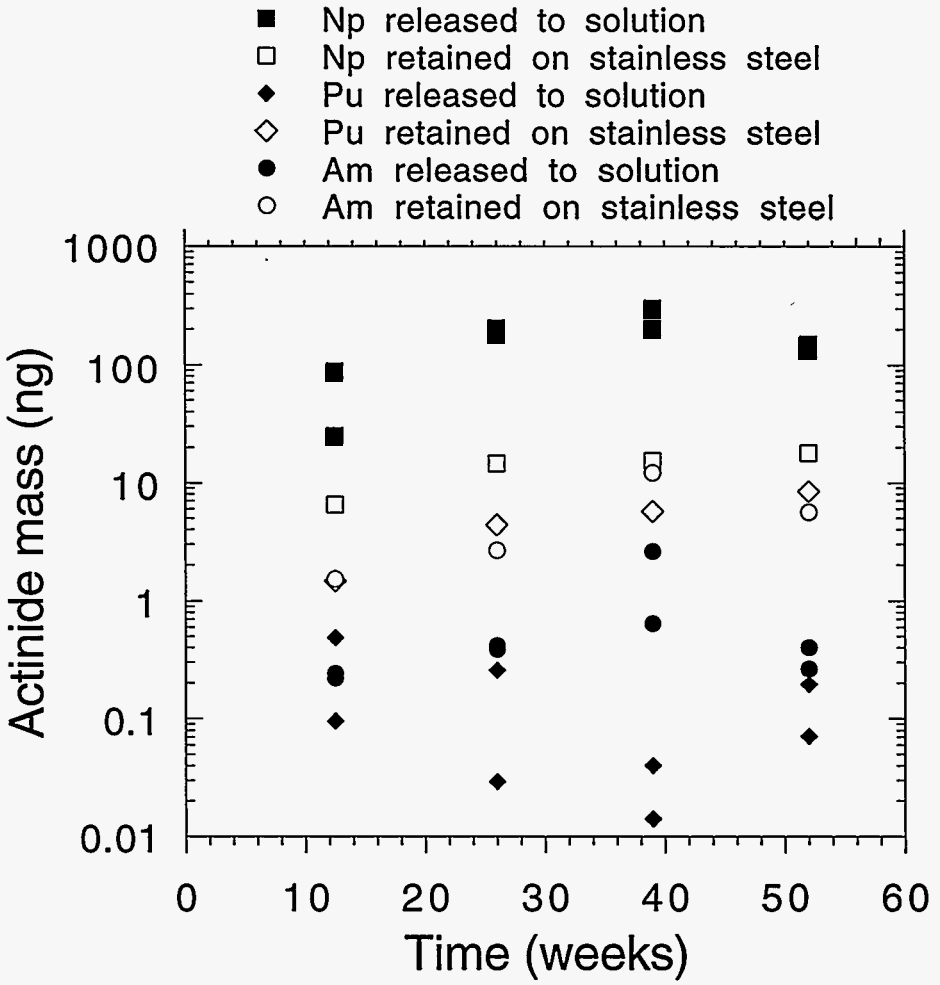

Fig. 20. Mass of Actinides Released to Solution (solid symbols) and Retained on the Stainless Steel (open symbols) as Determined by High-Resolution α-Spectroscopy

retainers, including elements incorporated into alteration phases on the stainless steel. This retainer strip represents additional reaction of the waste glass that had not yet been released from the WPA. Note that far less neptunium was deposited on the stainless steel than was being released into solution, a reflection of the tendency of this element to remain in solution and not form alteration phases. The plutonium and americium showed a marked tendency to be retained on the stainless steel at all test times at levels comparable to or exceeding the release to solution.

When comparing elements present in the glass in widely varying concentrations, it is useful to consider the normalized release, $N_i = \frac{M_i}{(c_i\ A)}$, where M_i is the mass of element i released from the sample, c_i is the atomic fraction of element i in the source glass, and A is the surface area of the glass monolith (1.36×10^{-3} m^2). Elements retained on the stainless steel are not considered released from the WPA; however, they are released from the glass and it is useful to use the standard normalization above for comparative purposes, where we can replace M_i with the mass transferred to the stainless steel. The normalized transfer of the elements lithium, thorium, uranium, neptunium, plutonium, and americium to the stainless steel retainer as determined with ICP/MS appears in Fig. 21. Most of the elements are present at comparable levels in all samples. Uranium and, to a lesser degree, americium display a greater tendency to

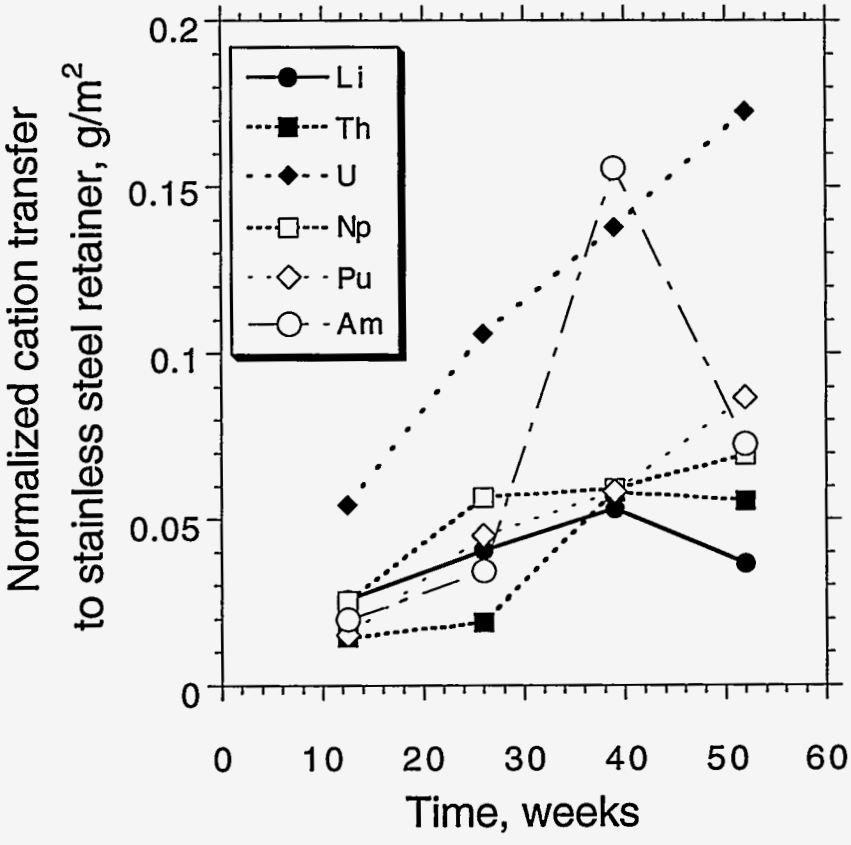

Fig. 21. Normalized Transfer of Selected Elements to the Stainless Steel Retainer. These data are from an acid strip of the retainer components and do not include elements released to solution.

be retained on stainless steel. The relatively low values for thorium probably reflect its retention on the surface of the glass (probably as brockite or another mineral), not that it remains in solution. Since few uranium alteration phases were observed, the high uranium retention on the stainless steel is probably due to sorption rather than accumulation of an alteration phase. Americium, present in the glass at much lower levels, is known [13] to be incorporated into the widespread brockite particles that were frequently observed on the stainless steel during the SEM examination. Its appearance at much larger normalized concentrations than thorium may indicate additional sorption onto the stainless steel.

The raw data from the ICP/MS of the acid strip solutions appear in Table 7, along with calculated mass releases. The normalized transfers shown in Fig. 21 were calculated by use of the above definition with the atomic fractions determined from the oxide weight percentages in Table 3 and the atomic masses. The high retention of uranium and americium, as well as the relatively high retention of plutonium and americium compared to solution release values illustrates the importance of synergistic reactions among the test components under these conditions.

C. Analytical Transmission Electron Microscopy Findings

1. Formation of Smectite Clay Layers

The most common alteration product to form on the surface of glass reacted with water is a clay, and owing to the relatively high iron and low magnesium content of waste glass, smectite clays are most frequently observed. Glass is a metastable state of matter and reverts to a crystalline phase (or even several coexisting crystalline phases) if provided with a mechanism for atomic transport. The glass-water interface provides an environment with multiple transport mechanisms: diffusion of non-network-forming elements (such as alkalis and transition metals) into solution, erosion of the Si-O network to form a gel layer plus silicic acid in solution, and precipitation of secondary crystalline phases. Smectite clays form both within the dissolving gel layer as remaining atoms rearrange and from solution, where colloids form and eventually reprecipitate on the surface of the glass. Clays can also grow on the surface directly from dissolved ions in solution. These various mechanisms can lead to complex patterns in the structure of the clays. Clays have a layered network structure that is apparent in many of the

Table 7. Calculated Total Cation Masses from ICP/MS in the 304L ss Acid Strip Solution

		Calculated Cations Retained (ng)					
Test No.	Test Duration (weeks)	Li	Th	U	Np	Pu	Am
N3#2 ss-AS	12.5	468	567	343	6.5	1.47	1.53
N3#4 ss-AS	26	737	745	669	14.6	4.38	2.66
N3#6 ss-AS	39	967	2284	870	15.3	5.67	12.05
N3#7 ss-AS	52	667	2180	1093	18.0	8.43	5.63

AEM micrographs; however, they tend not to retain many of the elements present in the original glass. In particular, alkali metals, rare earths, thorium, and uranium are not retained in the clay structure at levels near those in the source glass. Boron, lithium, and neptunium are highly soluble and are generally released to solution rather than retained in the clay; the relatively insoluble plutonium and americium are observed to segregate into certain alteration phases such as the brockite as well as sorb onto the clay [13].

The N3#1 samples had formed only a thin clay layer (< 50 nm) upon their top and bottom surfaces after 12.5 weeks of testing (Figs. 22a-b). The clay in Fig. 22a, from the top surface of N3#1, was not highly ordered and consisted of a few atomic layers of smectite clay oriented parallel to the glass surface. The clay in Fig. 22b, from the N3#1 bottom surface, had initial stages of wispy clay protruding perpendicularly from its surface, a rare image of the initial formation of the backbone structure often observed in thicker clay alteration layers (see, for example, Abrajano et al. [11] or Fortner et al. [14]. After 39 weeks, the N3#5 glass had developed a substantial clay layer (Figs. 22c-e), exceeding 500 nm in places and often having a well-defined backbone (see especially Fig. 22d). As the glass etches beneath the clay, a void develops between the clay backbone marking the original glass surface and the etched glass, allowing new clay to form in between. It is this growth pattern that leads to the backbone appearance of the thicker clay layers. The clay has a much simpler elemental composition than the glass, being deficient in alkalis, uranium, and thorium and somewhat enriched in iron, aluminum, and magnesium. Also note an unusual thorium-titanium-iron-silicate secondary phase, distinct from the clay, appearing between the glass and the clay in the micrograph of the 39-week test (Fig. 22d). This thorium-titanium-iron-silicate phase appears to be completely amorphous, giving no crystalline diffraction pattern whenever it is observed, and is probably related to the metamict minerals chevkinite or thorutite. Note the extremely minute dimensions of these particles, generally only a few nanometers across, at best occurring in clumps a few tens of nanometers across. They were not detected during SEM because of their extremely small size and location beneath the clay layer. This thorium-titanium-iron-silicate phase is discussed in greater detail in Section III.C.2.

The role of clay layers in glass corrosion is not well understood. They result from restructuring of the glass network as water diffuses into the glass, breaking bonds and allowing the atoms to rearrange. Thus, they do not cause glass corrosion to accelerate, as is observed with the appearance of zeolite in static tests [15]. While some researchers suggest that the clay may have a role as a protective layer, this is not widely accepted [15]. In the present samples, the clay is quite permeable; it allows transport of soluble elements but does trap some colloidal phases as long as the layer remains intact. An examination of a specimen from the top center of the N3#3 glass (Fig. 23) revealed a region where clay had either been spalled away (this region would have been directly under the injected water during testing) or otherwise mechanically separated from the glass. The tremendous apparent increase in roughening of the glass in the absence of an attached clay layer is indicative of the etching that occurs beneath the clay layer.

2. Formation of Alteration Phases

A major finding on the bottom surfaces of the glass monoliths was a substantial iron-rich layer that had formed on the glass under the clay layer where the glass had contacted the stainless steel holder (Figs. 24 and 25). This iron-rich layer was only 50-100 nm thick after 52 weeks of testing (Fig. 25), which explains why (as discussed in Sec. III.A.2) it was difficult to get a detailed picture and EDS of this layer via SEM, even though it was visible optically. This reaction suggests that sensitized stainless steel, a source of dissolved iron, may cause additional acceleration of the glass degradation. The iron layers were amorphous or mesomorphic, suggesting that they are iron oxide or iron oxyhydroxides, which are often found intermixed with iron-rich clay minerals [16].

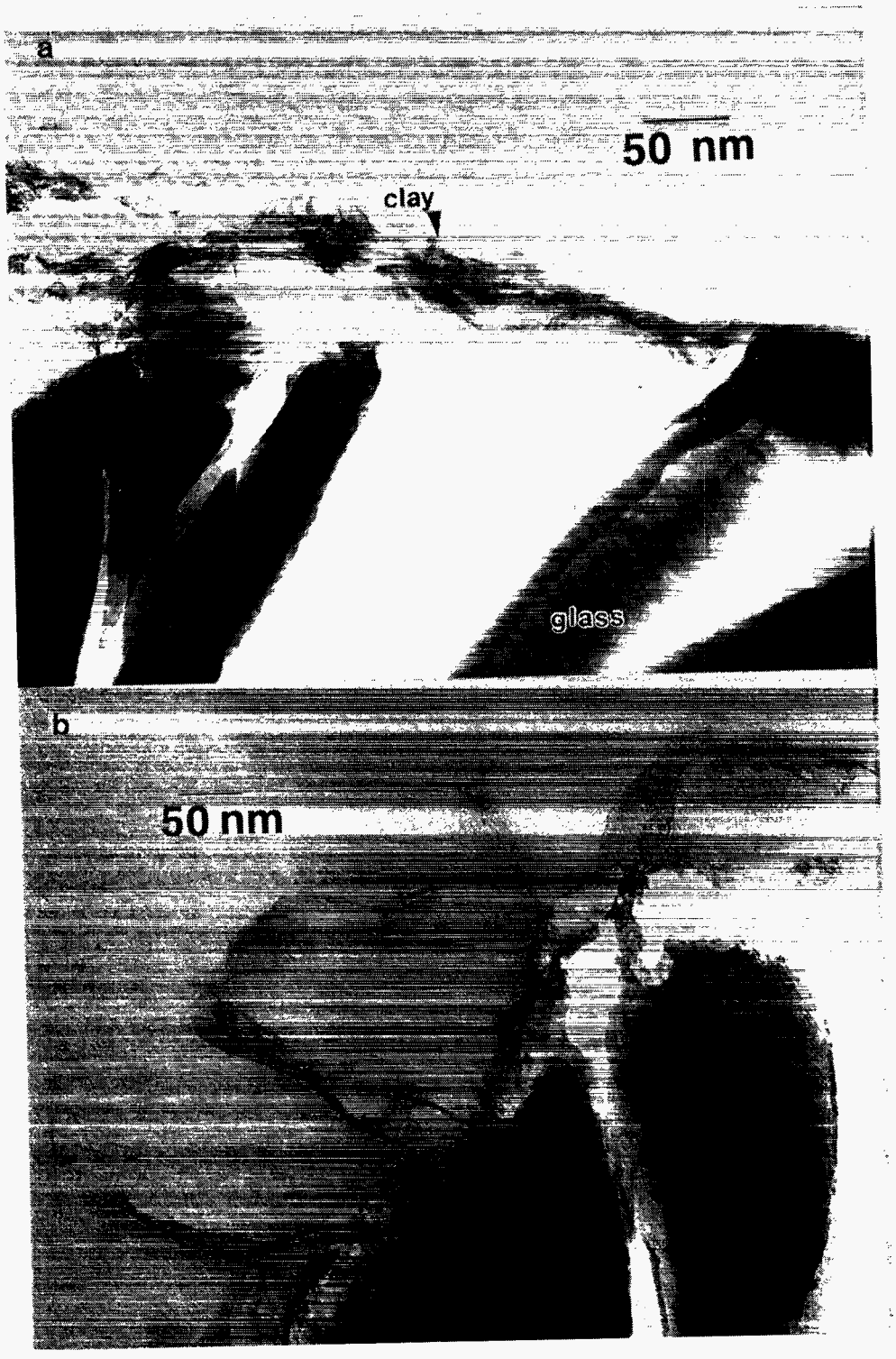

Fig. 22. Smectite Clay Formation on the N3 Glass Components as Examined by AEM of Thin Sections. (a) After 12-1/2 weeks of testing, a very thin (~20 nm) layer of clay had formed on the top surface of the N3#1 glass. (b) The bottom surface of the N3#1 had a similar thin surface layer of clay, with wisps of solution-grown clay extending perpendicularly from the surface.

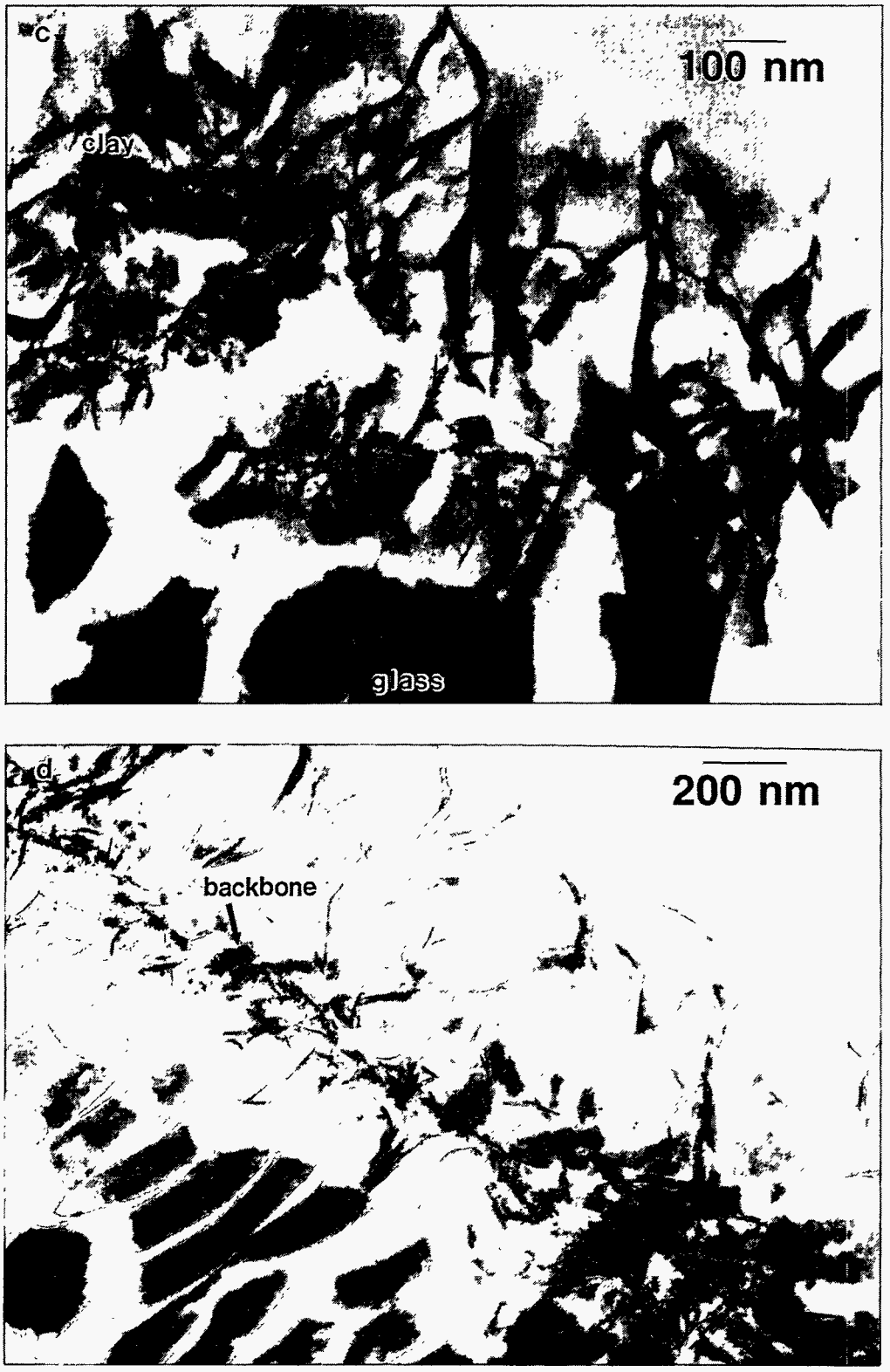

Fig. 22 (contd.) (c) By 39 weeks, the clay exceeded 500 nm thickness in some areas on the top surface of the N3#5 glass. (d) The clay layer on the bottom of the N3#5 glass exhibited a characteristic "backbone" structure.

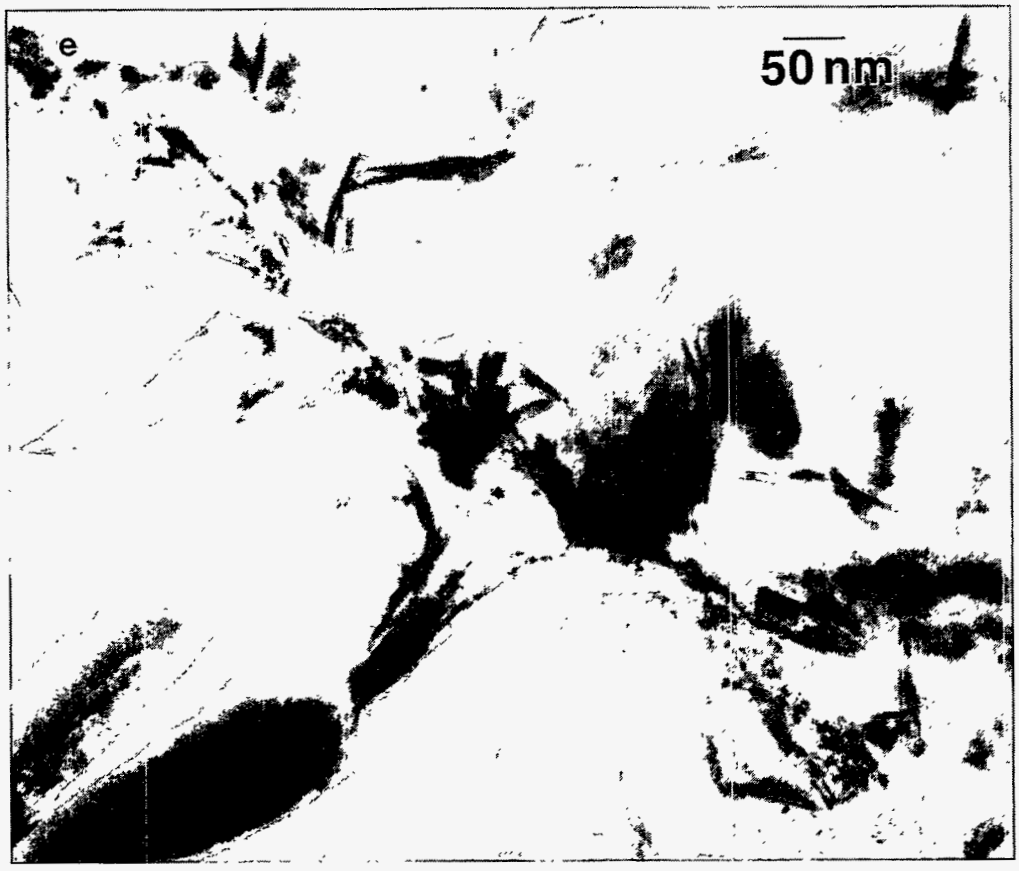

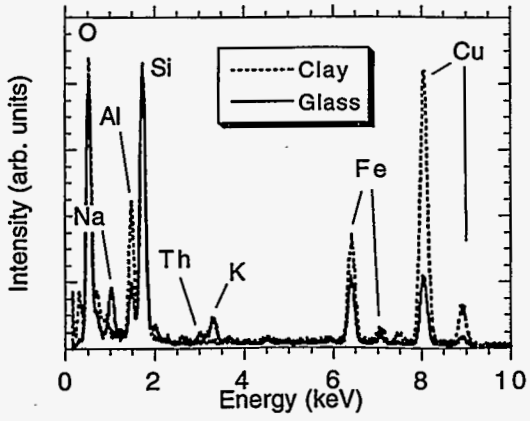

Fig. 22 (contd.) (e) Detail of (d). Note the presence of colloidal precipitates between the glass and the clay backbone; they were rich in thorium, iron, and titanium. (f) EDS spectra, normalized to Si-Kα intensity for comparison, of the clay and glass from the N3#8 top surface. Note the enrichment of Al and Fe and the depletion of Na, K, and Th in the clay layer. This compositional difference was typical of all clay layers that did not contain other alteration phases. The copper (Cu) peaks in the EDS spectra are artifacts of the AEM sample mount.

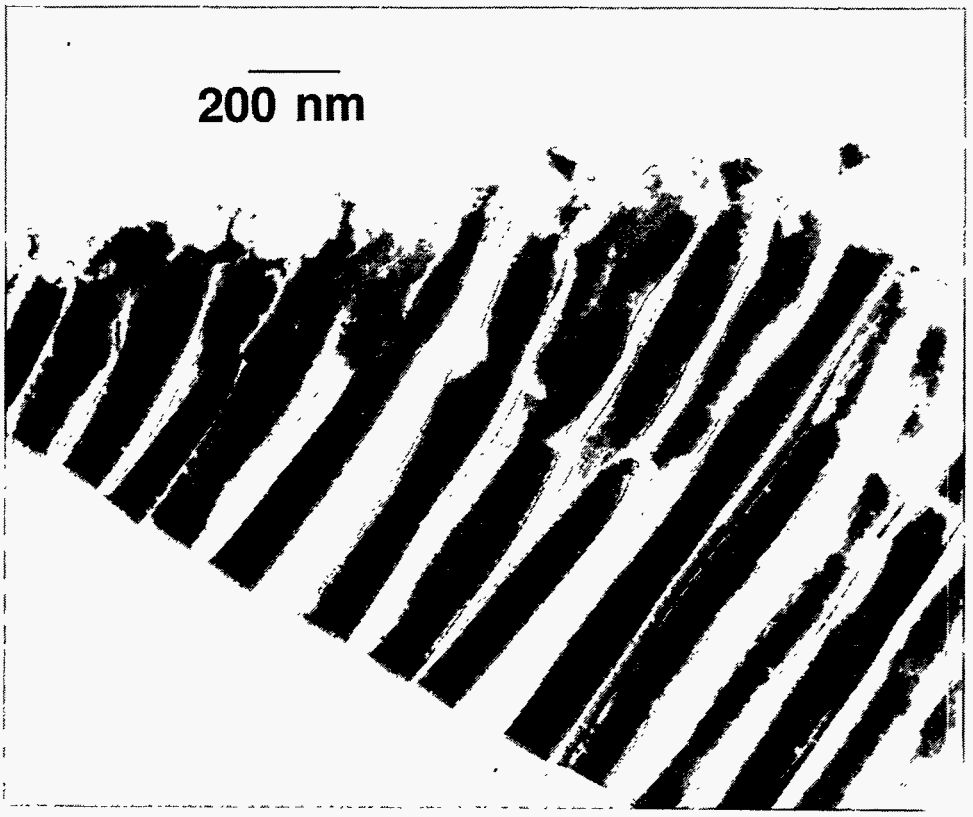

Fig. 23. AEM Micrograph of Pitted Glass without an Attached Clay Layer from the Central Area of the N3#3 Glass Monolith Top

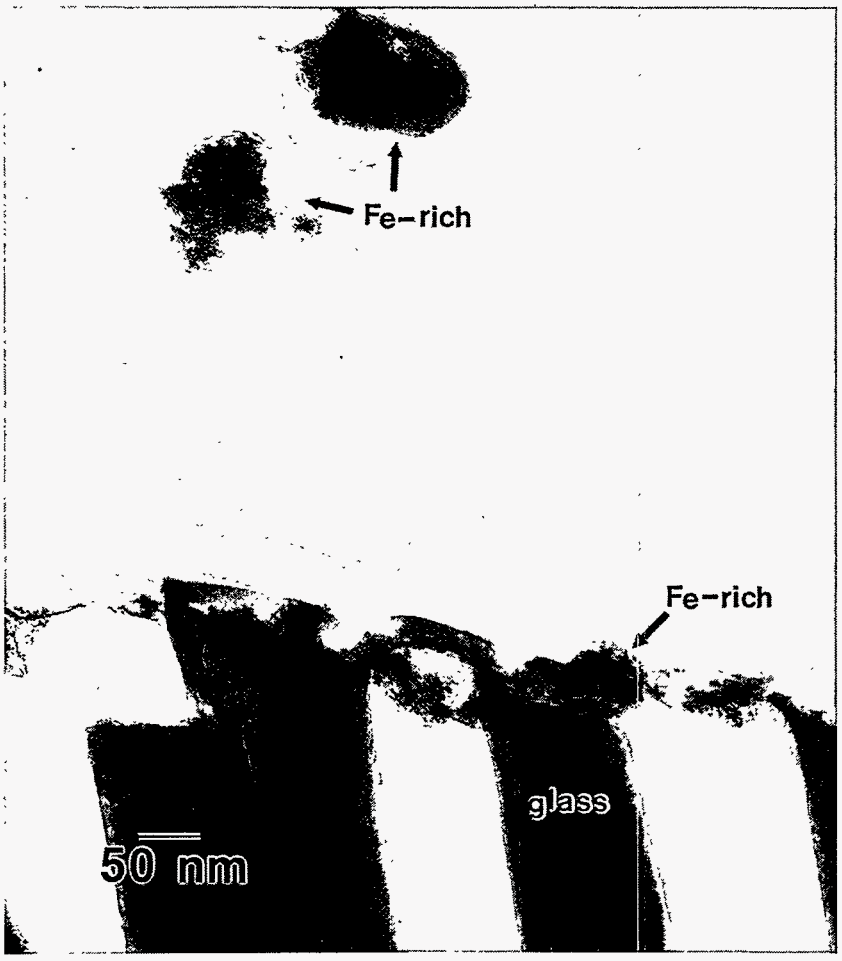

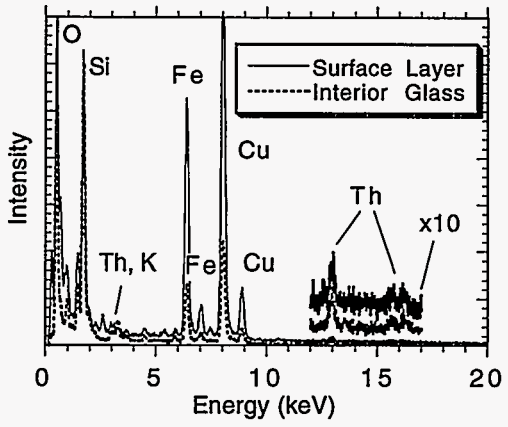

Fig. 24. AEM Micrograph (Above) from an Area of the Bottom Surface of N3#1 That Had Reacted with the Stainless Steel near a Weld. There is very little smectite clay, but an iron-rich layer is visible on the glass surface and some detached colloid-sized iron-silicate particles are visible above the surface. The EDS spectra (below), normalized to Si-Kα intensity, of surface layer and interior glass. The copper (Cu) peaks in the EDS spectra are artifacts of the AEM sample mount.

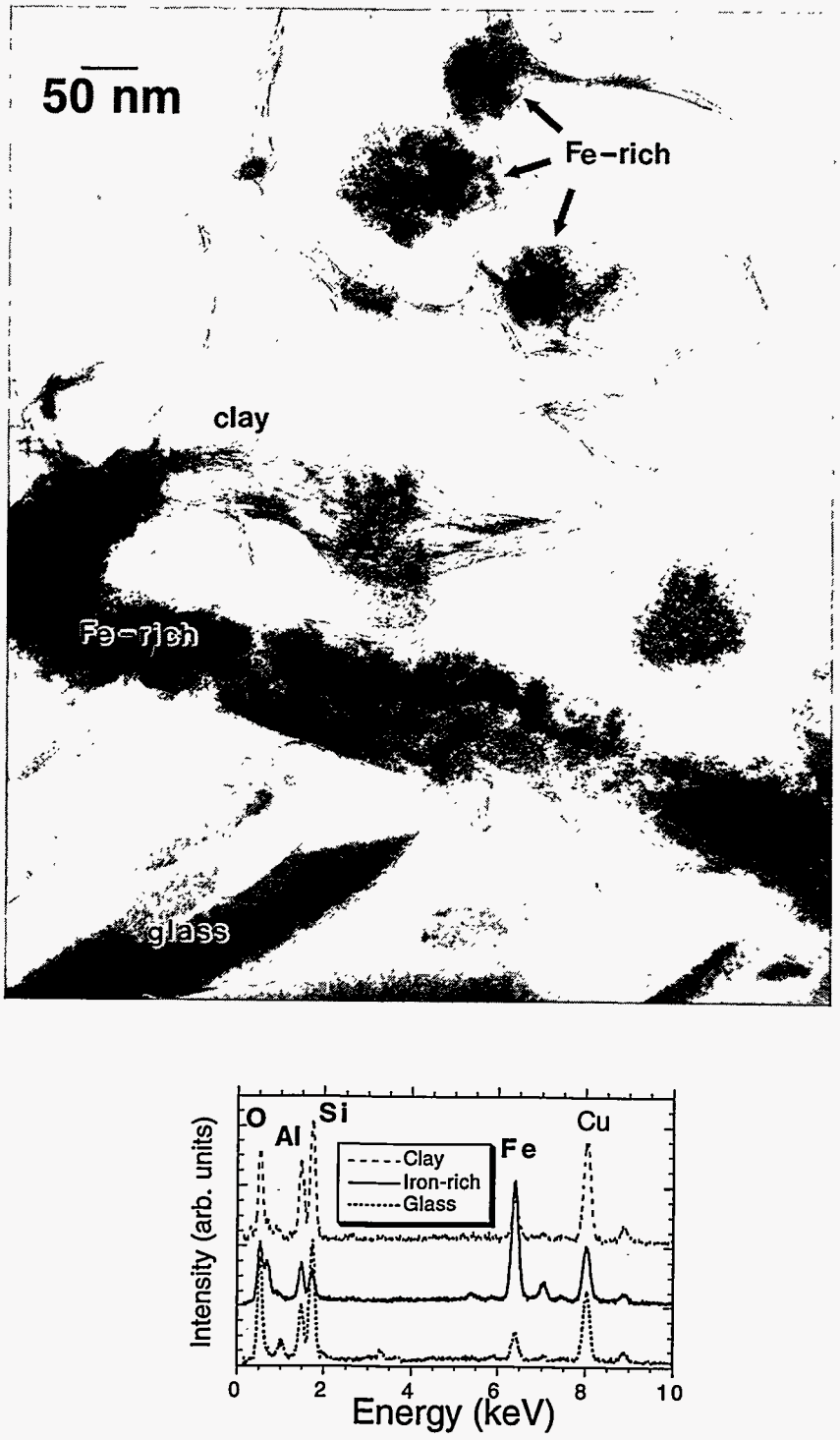

Fig. 25. AEM Micrograph (Above) of Layered Structure Containing Clay, an Iron-Rich Precipitate, and Glass on a Portion of the N3#8 Bottom Surface that had Contacted the Stainless Steel Retainer near a Welded Retainer Post and Their EDS Spectra. Neither the iron-rich nor the clay layers retained substantial Th. The copper (Cu) peaks in the EDS spectra are artifacts of the AEM sample mount. Compare with Fig. 24.

Crystalline iron silicates were also observed; one particle from the top surface of N3#3 was identified by electron diffraction as fayalite (Fe_2SiO_4, Fig. 26 and Table 8). Generally, though, the diffraction patterns from iron-bearing surface material were weak or diffuse, typical of poorly-crystallized matter, and could not be identified positively by the observed diffraction spots.

Brockite particles were ubiquitous, generally imbedded in the surface clay layer and sometimes exceeding 200 nm in length (Figs. 27-29). Recall that much larger particles having this composition were observed with the SEM, the largest being over 3 μm across (Fig. 13). There appears to be a correlation between the largest brockite particle observed on a surface and the duration of the test from which it came, making it unlikely that brockite is a quench phase. Small brockite particles, often 50 nm or less, are found on all test surfaces examined, suggesting that there is continuous nucleation and growth of this phase. In contrast, the smectite-type clay grows as a continuous phase with time, having nucleated on the original glass surface. Electron diffraction confirmed the brockite structure in at least two samples (Table 9 and Fig. 30). Brockite is a member of the rhabdophane mineral group and is structurally similar to members of the monazite mineral group. Interestingly, monazite minerals themselves have been considered as crystalline waste forms for disposal of low-level radioactive waste [18]. Brockite is known to incorporate rare earth elements (REEs) (La, Ce, Nd) and uranium [14,19], as well as americium and possibly plutonium [13] into its crystal structure. Its appearance as an alteration phase may explain the low initial release rates of actinides from the N3 tests [2,3]. Figures 29a and 29b are EELS spectra for the REEs and actinides in this phase. By estimating the relative concentrations from the integrated EELS peak heights and their known cross sections [20], it can be seen that the REEs are partitioned into the brockite in rough proportion to their concentrations in the original glass. Furthermore, the Ce-$M_{4,5}$ edges appear to be shifted to lower energy by ~2 eV from the reference CeO_2 and the ratio of the M_4 to M_5 peak intensities (Fig. 29c) are consistent with cerium being in the +3 oxidation state, rather than the +4 oxidation state of thorium [21]. The ATM-10 glass contains minute levels of americium and plutonium (Table 3), and brockite is known to entrain transuranic elements [13]. The intensities of the Nd- $M_{4,5}$ and Ce-$M_{4,5}$ EELS edges from the brockite indicate that the plutonium and americium $M_{4,5}$ edges may have been observable had this element partitioned in the same manner as the REEs. Despite the excellent signal-to-noise, plutonium was not observed. The plutonium and americium are presumed, then, to have partitioned into the brockite in proportion to the thorium, making it undetectable at three orders of magnitude lower concentration. This contrast between the behavior of the REEs and the actinides suggests that the use of "surrogate" elements, in lieu of the actual actinides, should be viewed with a certain degree of skepticism. The rest of the plutonium and americium from the reacted glass, then, is either in the clay at undetectable levels, on the metal test components, or in solution.

The other thorium-bearing phase containing substantial iron and titanium, mentioned earlier in connection with the smectite clay (Figs. 22 and 28), was observed within voids or pits in the glass, especially in voided regions between the glass and clay (Figs. 31-33). Based upon its composition and characteristic amorphous diffraction pattern (Fig. 34), it is probably related to the "amorphous" group minerals thorutite, $(Th,U,Ca)Ti_2O_6$ [23] or chevkinite $[(Ca,Ce,Th)_4(Fe,Mg)_2(Ti,Fe)_3Si_4O_{22}]$ [24], both described as amorphous and metamict, crystallizing after heating 1 hour at temperatures near 1000°C. This material, however, did not contain either significant lanthanide elements or calcium, as chevkinite does. It would, however, be arbitrary to identify this substance with a specific mineral, as amorphous materials are known to have a more variable composition than crystalline matter [25]. In Figs. 31 and 32, the thorutite-like material is trapped between the glass surface and the "spine" of the clay backbone. The thorutite-like material has also been observed within cracks or near-surface voids in the glass. This observation suggests that it either forms from colloids, collecting where the flow of liquid is restricted, or that it nucleates *in situ*, where stagnant liquid water concentrates dissolved cations. It appears that the clay is acting as a barrier to the escape of this thorium phase into

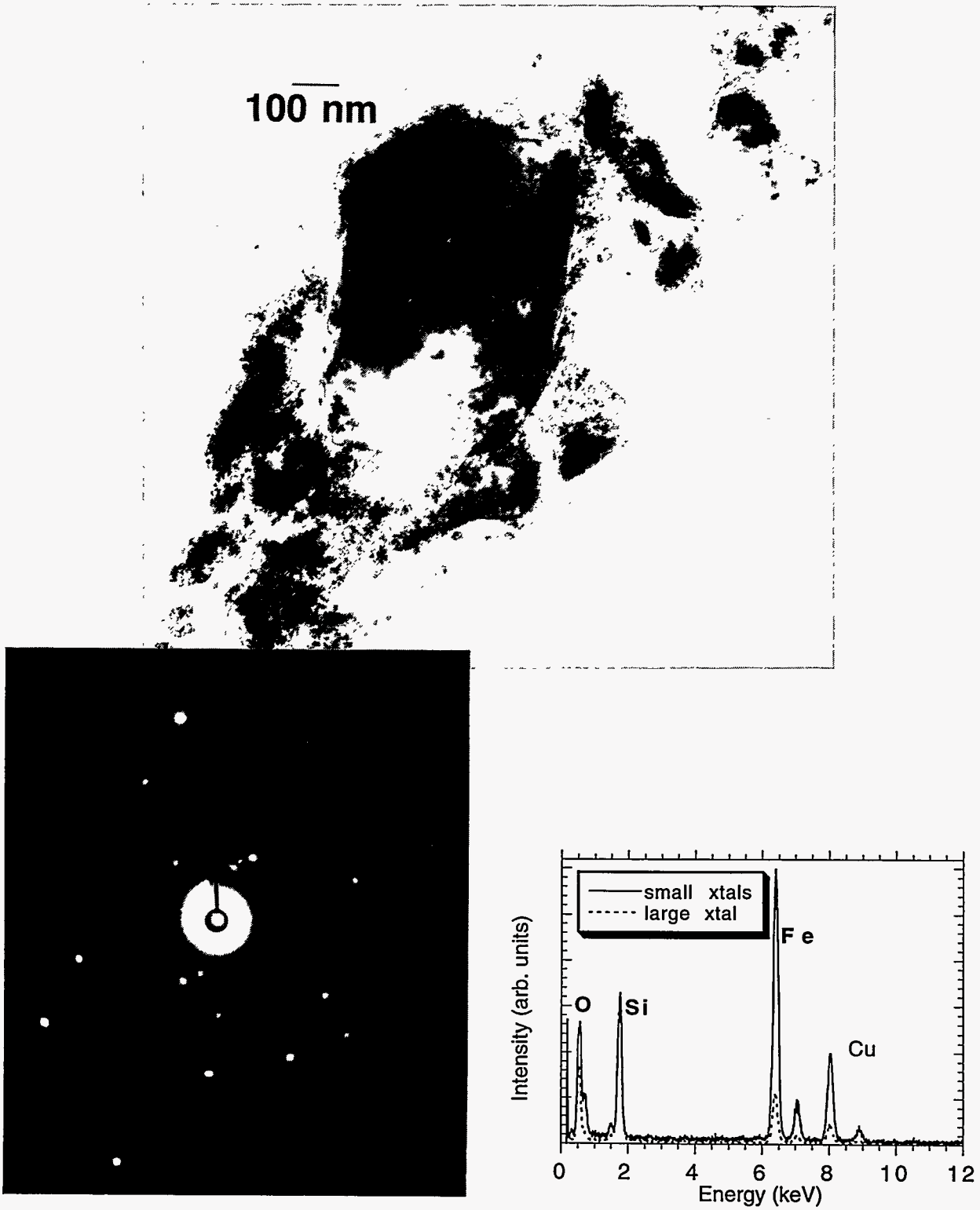

Fig. 26. Iron Silicate Crystals from the Top Surface of the N3#3 Glass Monolith. (a) Their AEM micrograph, (b) their electron diffraction pattern (measurements in Table 8), and (c) their EDS spectra, normalized to Si-Kα line, illustrating the variable composition of these particles.

Table 8. Electron Diffraction Results from the Top Surface of N3#3, Compared to JCPDS Data [17]. The pattern matches reasonably well with the iron-silicate mineral fayalite.[a]

Observed d Spacings C15076 (nm)	Fayalite Fe_2SiO_4 JCPDS 20-1139
	0.523, 0.438
0.40	0.398
	0.355
0.312	0.305
	0.2828, 0.2501
0.234	0.2307, 0.2348
	0.2192
0.197	0.1987
	0.1838
0.1682	0.1680
0.1536	0.1536

[a]Major observed reflections in **bold**.

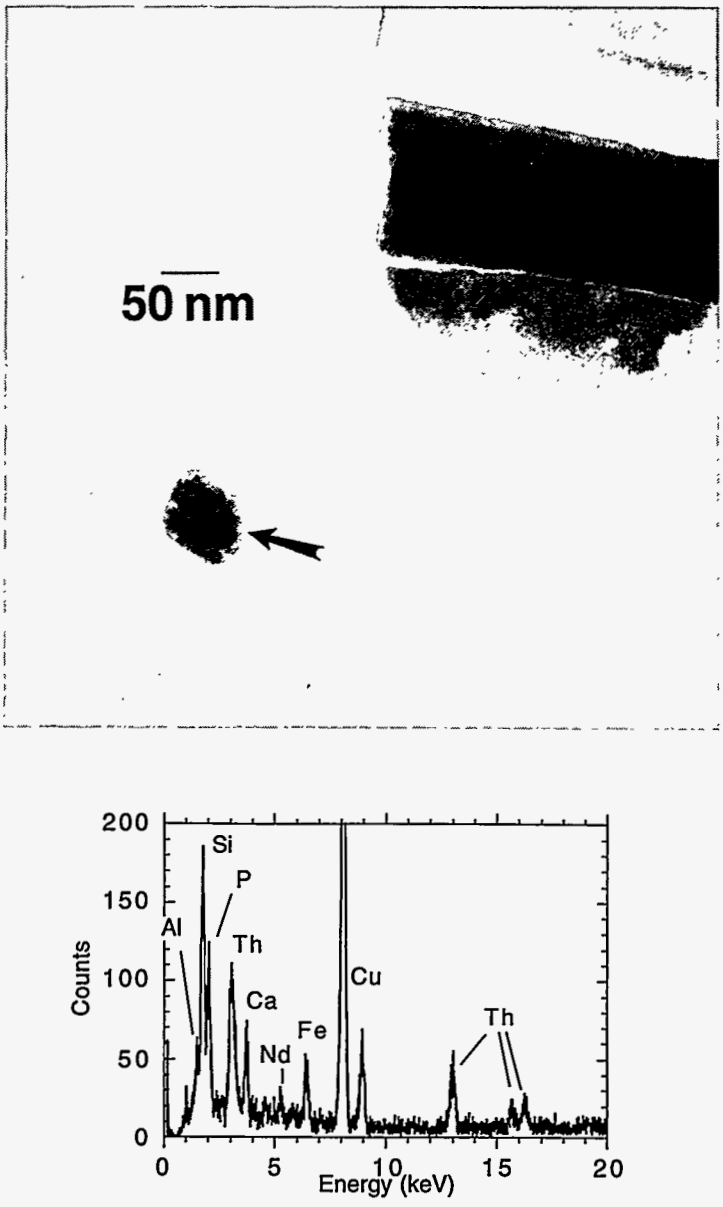

Fig. 27. AEM Micrograph (Above) and EDS Spectrum (Below) of Particle having Brockite Composition Found on the Top Surface of N3#1. This particle (indicated by the arrow) is detached from the glass, which is visible in the upper right. The copper (Cu) peaks in the EDS spectrum are artifacts of the AEM sample mount.

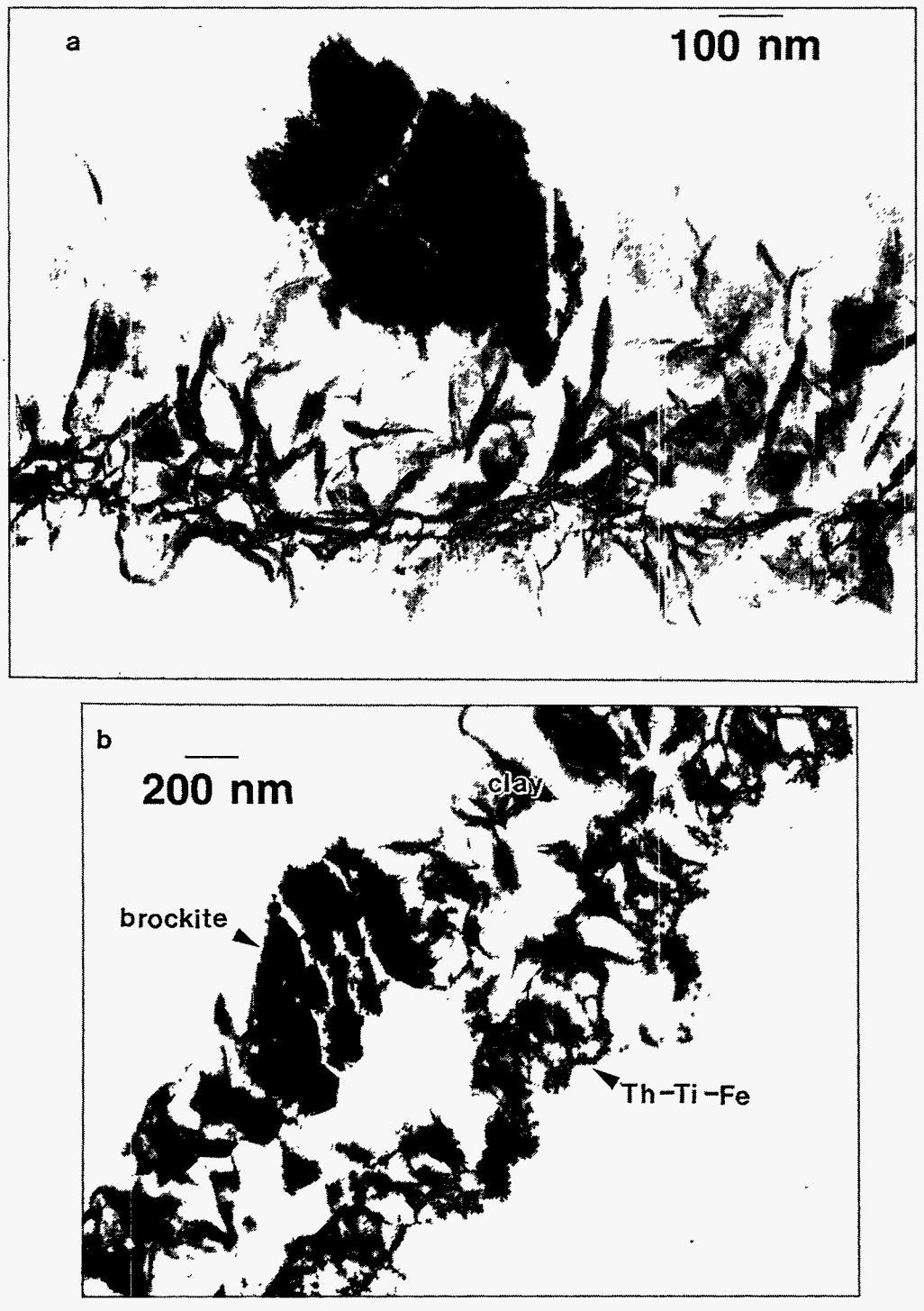

Fig. 28. AEM Micrographs of Brockite Particle Attached to Clay from the Top Surface of the (a) N3#5 and (b) N3#8 Glass Monoliths. The N3#5 brockite is on the outer surface; the glass (now detached) was originally opposite the particle. The N3#8 particle appears to be within the clay, although the glass, also now detached, was originally opposite side of the clay from this particle. Note the thorium-titanium-iron precipitates on the surface of the clay that had been attached to the glass.

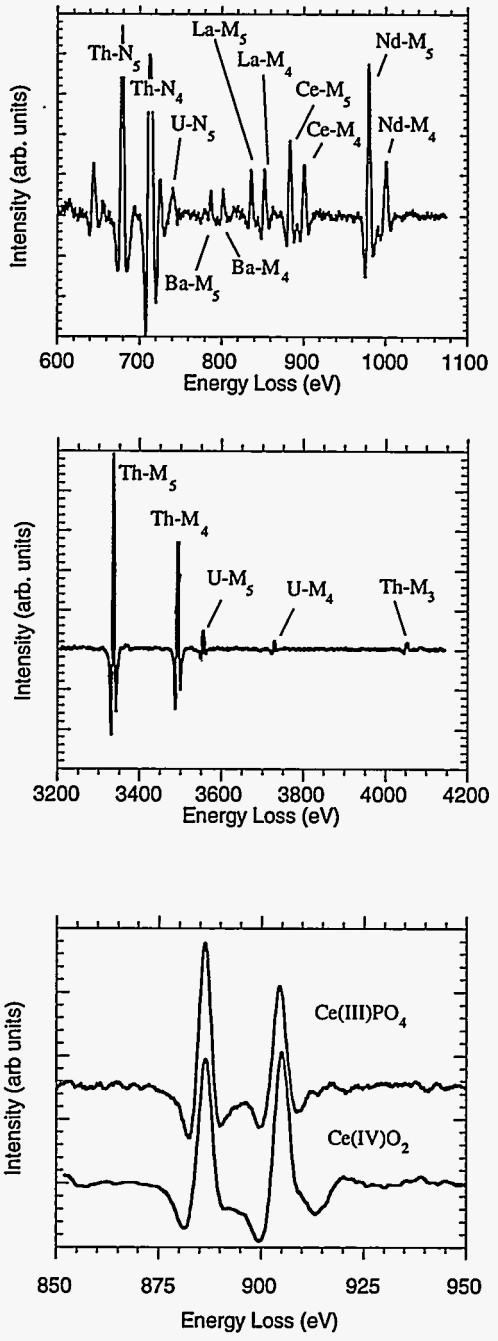

Fig. 29. EELS Spectra of the N3#8 Brockite Particle from Fig. 28 and of Reference Cerium Compounds. Spectra (a) and (b) show REE content and (b) actinide M-edges (transuranic elements are below detection limits), respectively. Spectrum (c) shows a comparison of Ce-$M_{4,5}$ edges in Ce^{+3} and Ce^{+4} compounds. Comparing the lineshapes with those in (a) indicates that cerium in the brockite is strictly in the +3 oxidation state.

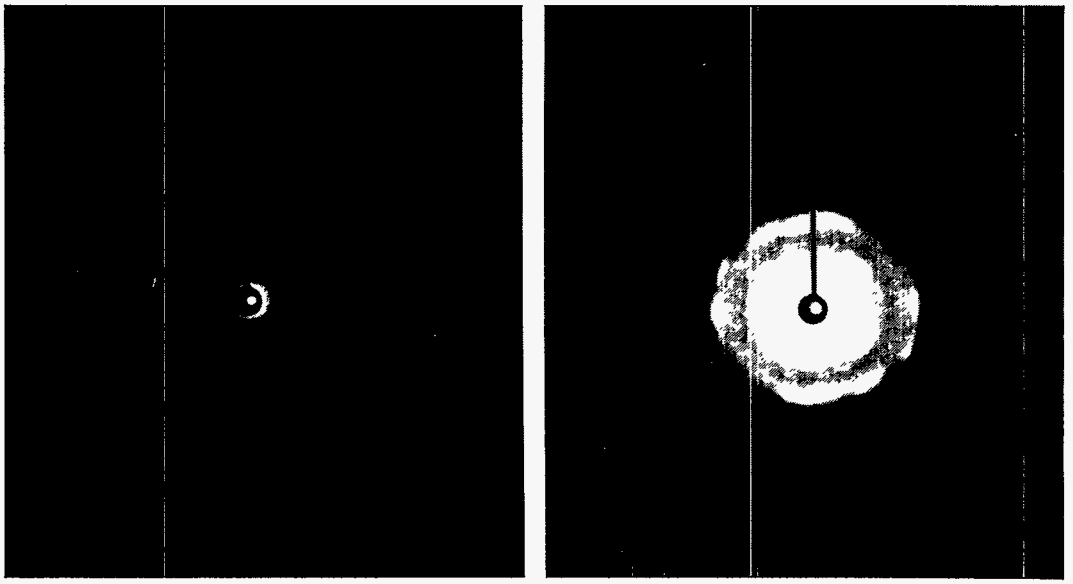

Fig. 30. Electron Diffraction Patterns of Brockite Particles from N3#8. The diffuse spots indicate partial amorphization. Most other brockite particles observed produced only the diffuse rings of completely amorphous material. The above diffraction patterns are indexed in Table 9 and compared with X-ray diffraction data from the minerals brockite and cheralite (a closely related mineral).

Table 9. Electron Diffraction from the Calcium-Thorium-Phosphate Phase Compared to Data from the JCPDS Reference [17][a,b]

Observed d Spacings (nm)		Literature d Spacings (nm)	
C14453[c]	C15808[c]	Brockite[d] JCPDS 15-248	Cheralite[e] JCPDS 33-1095
0.619		**0.606**	0.52
0.459	**0.447**	**0.437**	0.477, 0.4664
			4.073, 4.167
0.318	**0.326**	**0.347**	**0.3481**
			0.3277
	0.302	**0.303**	**0.3074**
0.293	**0.281**	**0.283**	0.2965, **0.2862**
0.248		**0.237**	0.2435
0.2226	**0.210**	**0.215**	0.2237
0.1926		**0.192**	0.1925
		0.186	
	0.174	**0.175**	
	0.166	**0.167**	

[a] The observed diffraction pattern more closely matches a brockite structure.

[b] Major reflections for mineral references ($I/I_0 \geq 30\%$) and most intense observed reflections are listed in **bold**.

[c] These labels refer to the serial number of the AEM film image.

[d] Brockite: nominally, (Ca, Th, Ln) $(PO_4) \cdot H_2O$, rhabdophane group, hexagonal system, space group $P6_222$. The reference, [19] gives the sample analysis as $Ca_{0.43}\ Sr_{0.03}\ Ba_{0.02}\ Th_{0.41}\ Ln_{0.11}\ (PO_4)_{0.83}\ (CO_3)_{0.17} \cdot 0.9\ H_2O$. Fisher and Meyrowitz determined that upon heating, the structure changes to that of the monazite group (as in cheralite).

[e] Cheralite: nominally, (Ln, Th, Ca, U) (PO_4, SiO_4) , monazite group, monoclinic system, space group P21/n. The reference, [22], give the sample composition by microprobe analysis (oxide wt. %) as CaO 5.99, PbO 1.15, ThO_2 31.64, U_3O_8 4.33, P_2O_5 27.10, SiO_2 2.08, Ce_2O_3 12.12, La_2O_3 5.19, Pr_2O_3 1.20. Nd_2O_3 5.91, Sm_2O_3 1.81, with trace levels of other lanthanides.

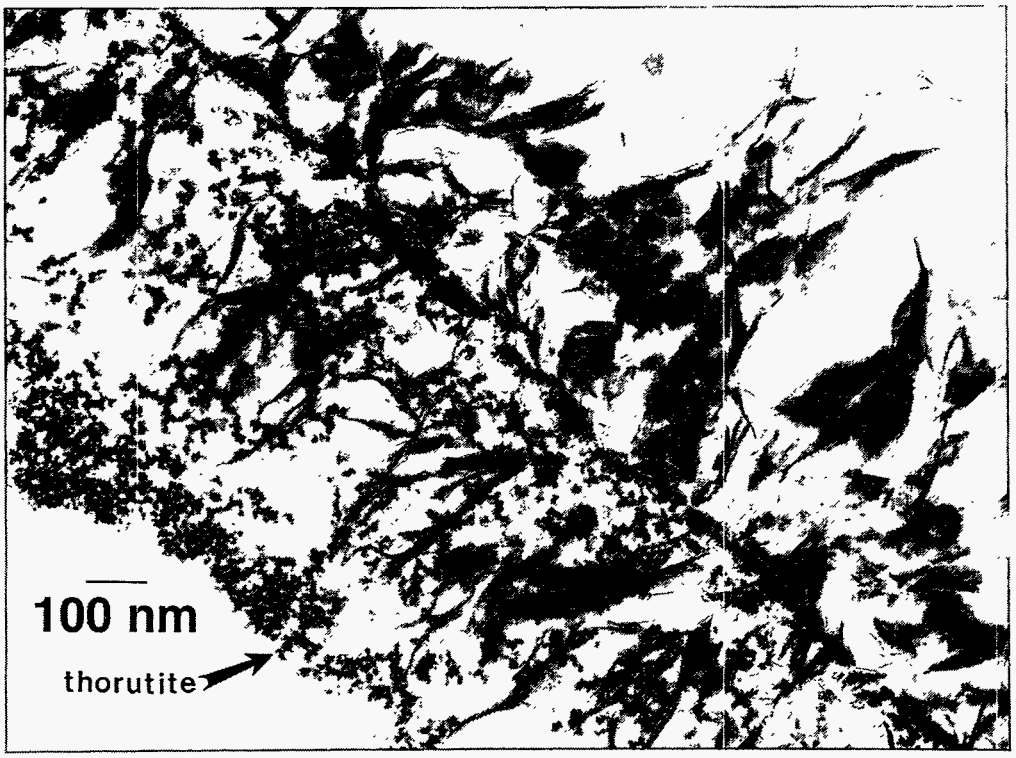

Fig. 31. AEM Micrograph of Clay from the Bottom of the N3#5 Glass Monolith Showing Copious Amounts of the Thorutite-Like (thorium and iron-rich) Material Trapped between the Clay Backbone and the Clay-Glass Interface. The glass, which was not attached to the clay in this region, was originally located on the side where the thorutite is deposited.

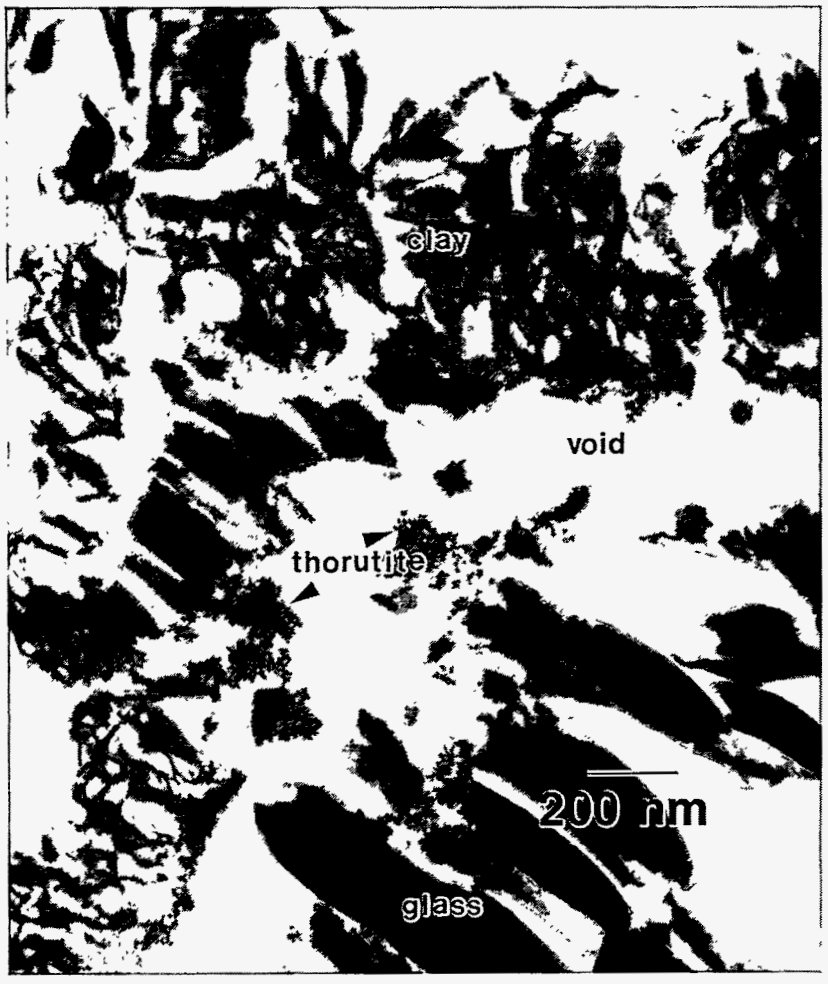

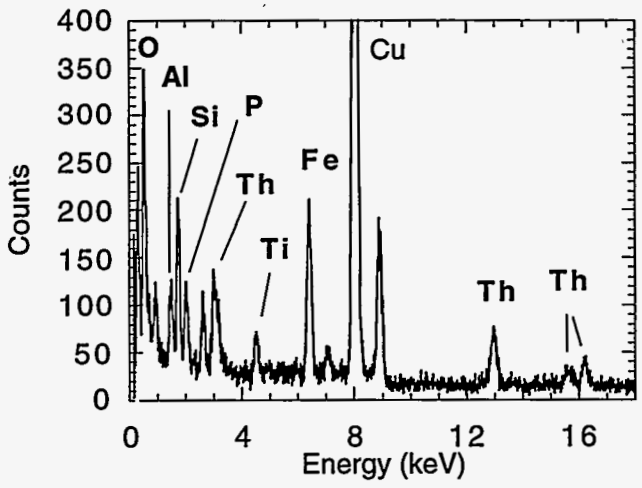

Fig. 32. AEM Micrograph (Above) of Clay and Glass from the Bottom of the N3#8 Glass Monolith Showing the Thorutite-Like Material Trapped between the Clay Backbone and the Clay-Glass Interface. Note also its presence around the voids in the glass. Below is an EDS spectrum of the thorutite-like material. The copper peak is an artifact of the sample mount.

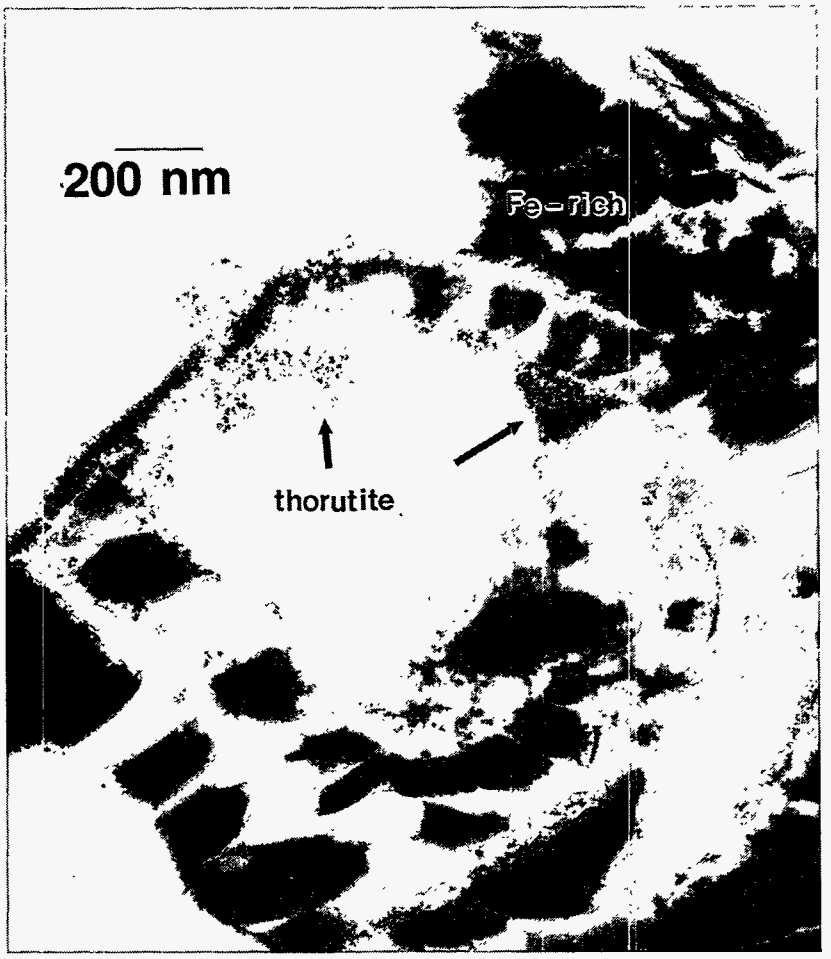

Fig. 33. AEM Micrograph Showing the Presence of the Thorutite-Like Material around a Void in the Glass under an Iron-Silicate Layer from the N3#8 Bottom Surface (see also Fig. 25)

solution; indeed, it may explain the extremely low normalized thorium release to solution in the long-term drip tests yet still in progress [3]. In Figs. 32 and 33, note the increased roughening of the glass surfaces in these void areas where the clay has separated from the glass (compare Fig. 23).

The thorutite-like phase did not contain any detectable rare earths (Fig. 35), further distinguishing it from the brockite. It is worth noting that both the brockite and the amorphous "thorutite" phases incorporated measurable uranium and probably entrained transuranics. This hypothesis is partly supported by previous work [13], where autoradiography and AEM were combined to identify a correlation between transuranic activity (americium) and the presence of brockite in leachate solution-borne clay colloids. The notion of transuranic entrainment in the brockite is also supported by the fact that the brockite often appeared amorphous or highly disordered—consistent with substantial radiation damage—whereas natural brockite minerals are generally crystalline, despite self-irradiation from the natural thorium and uranium over geologic time periods (Fig. 34).

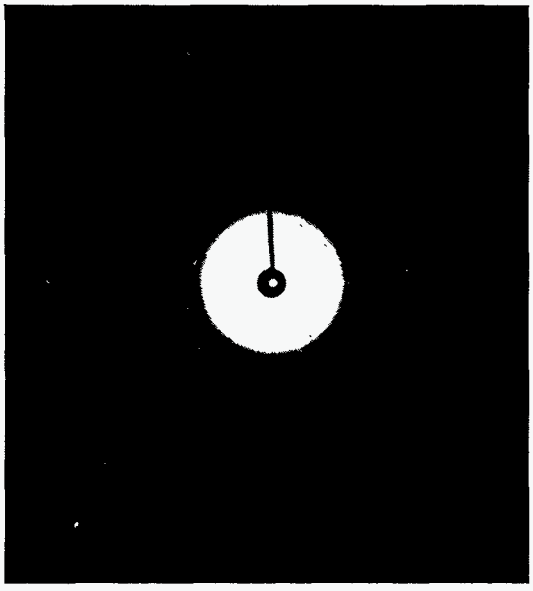

Fig. 34. Electron Diffraction from the Thorutite-Like Material was Always Characterized by Amorphous Diffuse Rings

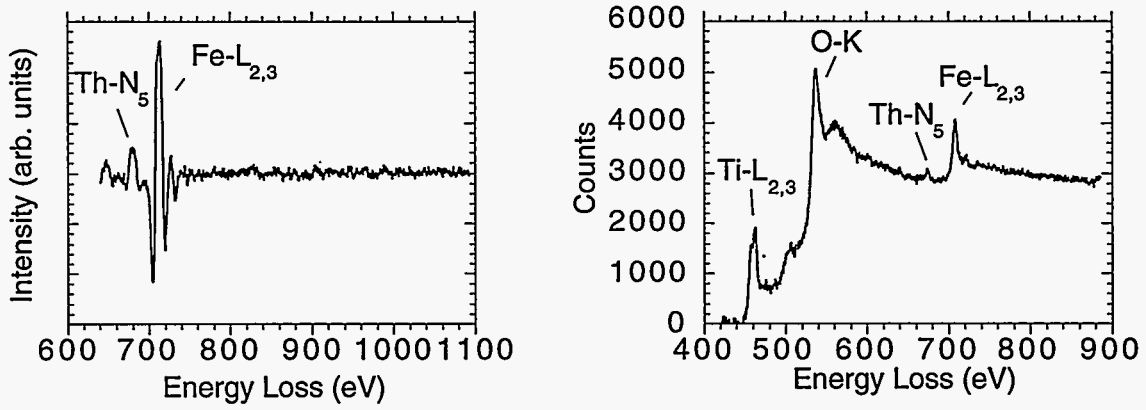

Fig. 35. The EELS Spectra of Thorutite-Like Material. It shows the lack of substantial amounts of rare earth elements: (a) A second derivative spectrum of the energy range where the M edges of REEs would occur (compare with Fig. 29); (b) a raw intensity spectrum showing the Ti, O, Th, and Fe edges as labeled.

IV. THE REACTION MECHANISM OF ATM-10 UNDER DRIP TEST CONDITIONS

In order to consider a mechanism for glass reaction, an initial understanding of glass structure, particularly the organization of the silica network and the role of network modifiers must be considered. An excellent description of the physics and thermodynamics of glassy condensed matter systems is given elsewhere [25]. More recently, Ellison et al. [26] discussed specifically the role of different chemical constituents in the structure of an alkali boro-aluminosilicate glass and their role on chemical durability. Readers are referred to these sources for the basic glass structure concepts which will be assumed in the following discussion. We restrict ourselves here to discussing the observed mechanism for the ATM-10 dissolution under unsaturated conditions, although it should be noted that many of the observations are general to glass-water systems.

Glass, being a metastable state of matter, can lower its configurational free energy by transforming into other, presumably crystalline, materials. For an alkali boro-aluminosilicate glass, particularly of the type considered for nuclear waste storage, configurational reorganization of an isolated sample (i.e., not contacting water) occurs so slowly as to be unobservable (we will not consider here possible diffusion and phase separation due to self-irradiation of radioactive glasses). However, upon contact with fluid water there is a sudden mechanism for ionic and molecular transport, allowing structural rearrangements that lower free energy and chemical potential gradients, and ultimately lead to crystallization and phase separation. Upon initial contact with water, the chemical potential gradients are steep, particularly for glass-forming components such as SiO_2 and B_2O_3, and the reaction progresses rapidly. This initial reaction rate is controlled by the glass composition and is referred to as forward rate of reaction [26,27]. At later times, the water approaches saturation of the rate-limiting components and the reaction rate slows considerably. Eventually a regime may occur where alteration phases precipitating from solution control the rate, which then increases considerably. Some glass design strategies purposely avoid compositions that would lead to a late-developing rapid reaction [27]. The drip test samples examined here all exhibit characteristics of Stage II progress. Stage III reaction had not occurred in the N3 Tests even after seven years [3,14]. A description of potential glass-water reaction mechanisms is given by Bates et al. [15]; a summary of the individual reactions that occur during glass corrosion appears in Table 10.

A. Infiltration of Water Into the Glass: The Gel Layer

The initial reaction of a fresh glass surface with water will be the diffusion of water into the glass surface region. In some previous research, the proposed initial reaction with water is a dissociation of water at the glass surface followed by ion exchange [28]; however, substantial evidence indicates that water diffuses into alkali silicate glass mostly as molecular water [29-31]. In fact, if dissociation of water into H^+ and OH^- accompanied by ion exchange was the rate-controlling mechanism, glass would react much faster than is observed, given the rate of water penetration into the glass [30]. It is the relatively low density of the continuous random network structure of glass [25] that allows water to penetrate by diffusion. Initially, water diffusion, hydration of the glass, network dissolution, and ion exchange occur to some degree simultaneously. As soluble elements (i.e., Li, B, Na) are released from the hydrated layer in the early stage of reaction, it transforms into a gel layer. The gel layer, then, is a hydrated amorphous layer at the glass surface that has a bulk composition similar to that of the glass but depleted of soluble elements. Our first examination of the samples was after 12-1/2 weeks of

Table 10. Reaction Mechanisms in Waste Glass Corrosion[a,b]

	Reaction	Nomenclature
1	$\equiv Si-O-Na + (H_2O)_{aq} \rightleftarrows \equiv Si-O^- + Na^+ + H_2O$	Diffusion
2	$\equiv Si-O-Na + H_3O^+ \rightleftarrows \equiv Si-OH + Na^+ + H_2O$	Ion exchange
3	$2(\equiv Si-O-Na) + H_2O \rightleftarrows 2(\equiv Si-OH) + Na_2O$	Hydrolysis reactions at nonbridging oxygen sites
4	$\equiv Si-O-Na + H_2O \rightleftarrows \equiv Si-OH + Na^+ + OH^-$	
5	$\equiv Si-O-Si\equiv + OH^- \rightleftarrows \equiv Si-OH + \equiv Si-O^-$	Network hydrolysis (forward reaction)
6	$\equiv Si-O-Si\equiv + H_2O \rightleftarrows \equiv Si-OH + \equiv Si-OH$	Condensation (reverse reaction)
7	$\equiv Si-O-\underset{\underset{OH}{\vert}}{\overset{\overset{OH}{\vert}}{Si}}-OH + OH^- \rightleftarrows \equiv Si-O^- + (H_4SiO_4)_{aq}$	Network dissolution (forward reaction
8	$\equiv Si-O-\underset{\underset{OH}{\vert}}{\overset{\overset{OH}{\vert}}{Si}}-OH + H_2O \rightleftarrows \equiv Si-OH + (H_4SiO_4)_{aq}$	Condensation (reverse reaction)

[a]From Bates et al. [15], based upon Abrajano et al. [32].

[b]Although the reactions are written explicitly for Si and Na, similar reactions occur for other network-forming and network-modifying elements [26].

testing, by which time the gel had already been transformed to clay. Previous examinations of reacted glasses with gel layers have shown that the layers are easily distinguished from the hydrated glass by the morphology in AEM micrographs [11]. The gel is less dense than the glass and has a textured appearance that was not observed in the N3 samples.

Examination of the N3 samples revealed clay alteration layers on all of the reacted glass surfaces, even at the shortest reaction time of 12-1/2 weeks (Fig. 22). No gel layer was visible in the micrographs, so an attempt to detect a residual gel layer with EDS elemental profile was done with AEM. The results of one such profile appear in Fig. 36, where the near-surface region and the interior glass from an N3#5 specimen were examined with EDS in the transmission electron microscope. The near-surface region examined is just under the clay alteration layer and within ~0.2 μm of the surface. Note how all of the elemental EDS peaks are well reproduced, with only a slight decrease in Na and the appearance of trace Cl in the near-surface spectrum. The presence of chlorine near the surface is considered evidence of hydration in AEM samples [33], as chlorine from solution will diffuse into a sample along with the water. A similar EDS profile of the near-surface glass on a specimen from N3#1 was done and appeared almost identical to that in Fig. 36; thus, there is no evidence for a substantial ion-exchange layer. Although the glass is presumably hydrated near the surface, no gel layer is present after the 12-1/2 weeks of the initial test terminations; it could only have been present at early in the reaction, probably as a precursor to the clay nucleation. The near-congruent dissolution at the glass surface strongly supports the concept that the breakdown of the silica network, not ion exchange, controls glass reaction after the gel layer has transformed into clay. The evidence indicates that the glass corrosion in the N3 drip tests is reaction-limited, not diffusion-limited.

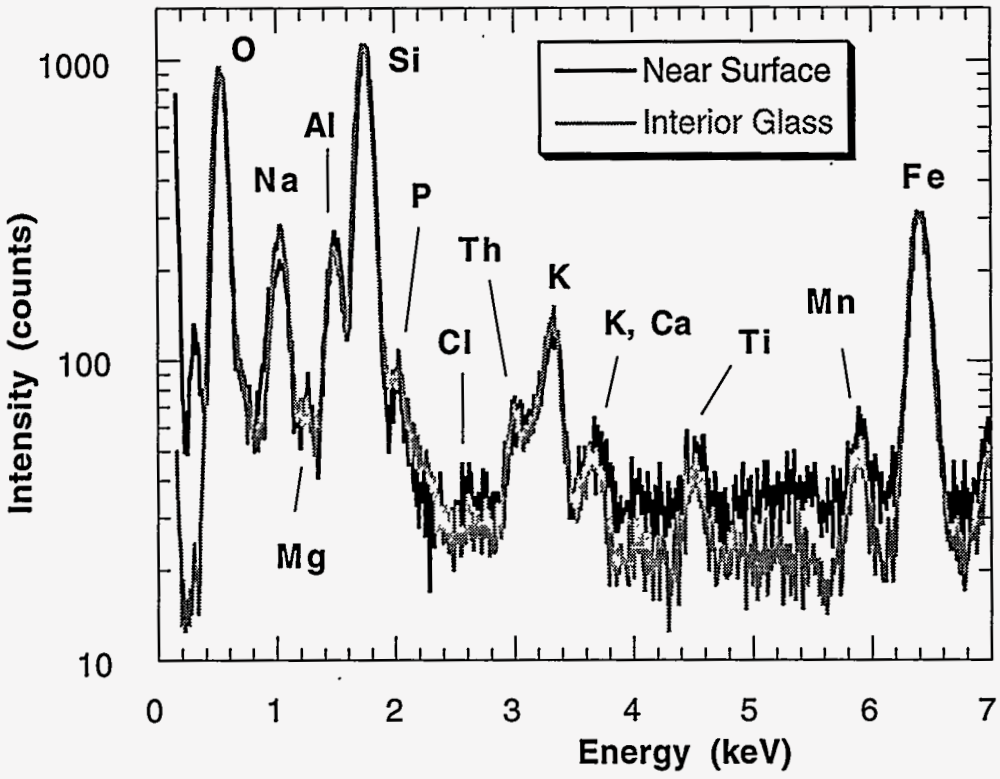

Fig. 36. The Near-Surface Region and the Interior Glass in a Specimen from N3#5 Examined by EDS in the Transmission Electron Microscope. The near-surface region is just under the clay alteration layer and within ~0.2 μm of the surface. Note how all of the peaks are well reproduced, with only a slight decrease in Na and the appearance of Cl in the near-surface spectrum. The near-surface spectrum was normalized by multiplication by a constant factor of ~2 for illustration purposes.

B. Formation of a Clay Layer

During the early reaction progress (prior to our earliest sample at 12-1/2 weeks), when the soluble elements are removed from the surface region of the glass, they leave behind a gel consisting of silanol groups and M^{ins}-O-Si non-bridging oxygen sites (where M^{ins} is a relatively insoluble metal). Eventually, the number of degrees of freedom of the system will exceed the mechanical constraints imposed by network bonding, and crystallization will occur; the balance between mechanical constraints and degrees of freedom germane to this process has been described in detail [34]. The major insoluble metal ion species in nuclear waste glasses are iron and aluminum, and the major alteration phase to form will have to readily accommodate these ions plus the silanol groups. Thus, although a number of hydrous layered silicates exist that can be formed at ambient temperature, the gel layer is observed to restructure into a smectite clay, generally having an Fe^{+3}-rich composition. Smectite clay minerals are composed of a layered structure of silicon-oxygen-metal (Al or Fe or other transition metals) sheets, separated by a rather large distance (over 1 nm, depending on hydration). These sheets are ordered in two dimensions, but are stacked randomly upon each other to produce the observed layered structure

[16]. Frequently, in the AEM micrographs the stacked layers are visible in profile, appearing as the "lattice fringes" in the recorded image.

The composition of the clay, as seen in Fig. 22f, is essentially that of the glass minus elements that are soluble or readily accommodated in other alteration phases. After the clay layer has formed, the gel layer is no longer observed in the N3 samples. However, studies using French SON68 glass [35] and generic waste glasses [11], each reacted under different conditions than those used in the N3 Tests, are examples where the gel layer is clearly observed. From these observations, we conclude that the clay forms initially very near the original surface of the glass in the present samples.

Once nucleated, the clay layer continues to grow and evolve. Growth occurs as the hydrated layer beneath the existing clay dissolves and the elements from solution saturate and reprecipitate onto the surface of the clay. This growth mechanism leads to the observed backbone structure of the clays in the N3 test glasses. The very thin clay layer at 12-1/2 weeks in N3#1 (Figs. 22a-b) has lattice planes oriented somewhat parallel to the surface, suggesting the original restructuring of the gel at the gel-water interface. The clay on the bottom of the N3#1 sample in Fig. 22b shows the very early stages of clay growth from elements in solution, as evidenced by the sparse wisps growing outward from the surface. At later times (Figs. 22c-e), the majority of the clay lattice is oriented perpendicular to the backbone layer, characteristic of growth from solution rather than solid state transformation. The included backbone of these extended layers marks the original glass surface, as seen from the N3#1 images in Figs. 22a and b. The transition from parallel to perpendicular lattice plane growth at the backbone is strikingly apparent in Fig. 22e. Since the glass is dissolving in a nearly congruent manner and the clay is permeable to the soluble elements, voids are frequently observed between the clay and glass. The etching of the glass beneath the clay continues in an irregular manner, leaving some points of contact between the clay and glass, holding the layer in place. Note that the clay grows outward from the backbone in both directions, that is, both out into solution and inward to fill the void left by the dissolving glass. This layer may spall away, however, as stress builds up in the structure and as the glass etches away beneath; this may be the origin of the clay colloid particles observed in solution from the N3 Drip Tests [3,13]. The composition of both the inner and outer growths of clay were indistinguishable with EDS, indicating that the solution conditions on both sides were similar. What generally distinguished the inner clay from the outer clay is the trapped thorutite material (Fig. 31), which will be retained by the clay layer as long as the clay layer remains intact. The inner clay, fed by continuous thorium, iron, and titanium from the reacting glass, continued to accumulate the thorutite material, which probably has a very low solubility, as indicated by its growth morphology as minute, distinct, noncrystalline particles. Note that both the thorutite and the brockite (Fig. 28) are attached to the clay. Thus, as the clay becomes detached from the waste package, these actinide-bearing phases may be released.

C. Precipitation of Alteration Phases from Solution

Sparingly soluble or insoluble elements that are not incorporated into the clay structure or that are present at levels beyond what can be accommodated by clay will precipitate as alteration phases on the reacted glass and nearby surfaces (such as the stainless steel retainer). As the solution composition evolves with time during glass and steel corrosion, so too will the assemblage of alteration phases evolve. The drip test used here does not lead to as rapid an evolution of solution chemistry as do static tests run at very high glass-surface-area-to-solution-volume (high S/V), such as the PCT or MCC-1 tests [25], because the slow exchange of water in contact with the glass does not reach (or may not ever reach) late-developing reaction conditions. Nevertheless, distinct trends in phase morphology, distribution, and abundance have been observed (as already demonstrated for the smectite clays). Perhaps more interesting than the changes with test duration, though, are the constants: (1) the smectite clays grow continuously on all glass surfaces, (2) brockite [(Ca, Th, rare earth)PO_4] appears as a major alteration phase

and appears to continuously nucleate, (3) sensitized 304L ss corrodes along with the glass, resulting in iron oxide and/or iron oxyhydroxide layers on the glass, and (4) the thorutite-like material, while not observed on the earlier tests, is observed in trapped volumes over the surfaces of the glass. Other phases associated with waste glass corrosion, such as zeolites, calcium silicates, and uranium silicates, were rarely or never observed on the N3 test samples. These later phases, however, serve to lower the rate-controlling silicic acid activity in solution and are often associated with advanced reaction [26].

The major constituents in the glass that are not either completely dissolved into solution or incorporated into the clay are thorium, phosphorous, calcium, uranium, and titanium. Excess iron is also present due to the corroding 304L ss. These elements, of course, constitute the two major (non-clay) alteration phases observed in the N3 Tests, namely brockite and amorphous thorutite. What has been observed in the AEM micrographs, in addition to the identification of these phases, is their morphology and distribution in the reacting layer. As noted above in the discussion of smectite clay layers, the thorutite appears in trapped volumes such as those between the clay backbone and the glass surface (Fig. 31) or in other voids (Fig. 33). Brockite, on the other hand, usually appears as discrete, mesomorphic particles on the outer surface of the clay or between the clay backbone and the outer clay surface. The thorutite and brockite often appear in close proximity to one another (bits of thorutite appear in both images of Fig. 28). The difference in conditions leading to the formation of each phase are apparently quite subtle and may be kinetic in nature. The highly dispersed arrangement of the minute thorutite particles in the clay beneath the backbone suggests that this phase is very insoluble (as may be expected for any titanium-containing phase). Although thermodynamic data is unavailable for brockite, a related phase called hydroxyapatite [$Ca_5(PO_4)_3OH$] is known to have a low solubility. The composition of the ATM-10 glass suggests that the thorutite precipitates rapidly until the solution is (locally) depleted of titanium, whereupon the remaining thorium is incorporated into the brockite.

D. The Interaction of Glass with Corroding Stainless Steel

Iron serves to accelerate glass reaction by either of two mechanisms: (1) metallic or oxidized iron serves as adsorption sites for silicic acid, and (2) iron can react with the silicic acid to form iron silicates or other compounds. Each of these interactions accelerate reaction by lowering the concentration of silicic acid in solution. Whereas sorption sites on the steel eventually saturate, the reaction to form compounds can continue until the glass (or iron) is completely consumed.

Previous work has concentrated largely on sorption studies, where the iron source was an oxide mineral (e.g., [36] and references therein). In the N3 Tests iron was supplied as a corroding metal, and the resultant interactions observed were more complex. The formation of iron-rich clays, while common in any iron-containing waste glass (most U.S. high-level waste glasses contain >5 wt % iron), has been accompanied by iron oxides and iron oxyhydroxides (Figs. 24 and 25), iron silicates (Fig. 26), and the iron-bearing thorutite material (Figs. 31-33). While none of these minerals has provided a sufficient "sink" for silicic acid to cause a late-developing, rapid reaction under drip test conditions, the synergy of the 304L ss and ATM-10 waste glass corroding together has clearly led to the development of phases that would rarely or never be observed under other, standard test conditions.

V. CONCLUSIONS

Analyses on samples from a long-term integrated test of actinide-doped West Valley ATM-10 reference waste glass under unsaturated post-containment conditions reveal complex interactions between the groundwater, the sensitized stainless steel waste form holder, and the glass. Alteration phases form that consist mainly of smectite clay, brockite, and an amorphous thorium iron titanium silicate, the latter two incorporating thorium, uranium, and possibly transuranics. The formation of these alteration phases may retard the initial release of the actinide elements; however, mechanical spalling of the reacted layer in the repository can release these materials as colloids that may be transported through groundwater. The importance of using a realistic test procedure and components is revealed by the resulting products and disposition of transuranics during glass corrosion.

ACKNOWLEDGMENTS

The authors would like to thank Nancy Dietz for valuable assistance with the AEM sample preparation and Stephen Wolf for alpha and gamma spectrometry and ICP/MS. The analyses presented herein were performed at Quality Assurance Level I and were subject to audit by both EM and ANL's OQA. The authors gratefully acknowledge the contributions of Roberta Riel and Sy Vogler for Quality Assurance coordination and assistance.

This work is supported by the U.S. Department of Energy, Office of Environmental Management, under Contract W-31-109-ENG-38.

REFERENCES

1. J. K. Bates and T. J. Gerding, *Application of the NNWSI Unsaturated Test Method to Actinide Doped SRL 165 Type Glass*, Argonne National Laboratory Report ANL-89/24 (1990).

2. J. K. Bates, J. A. Fortner, P. A. Finn, D. J. Wronkiewicz, J. C. Hoh, J. W. Emery, E. C. Buck, and S. F. Wolf, *Yucca Mountain Project- Argonne National Laboratory Annual Progress Report, FY 1994*, Argonne National Laboratory Report ANL-94/42 (1994).

3. J. A. Fortner and J. K. Bates, "Long Term Test Results from Unsaturated Testing of Actinide-Doped DWPF and WVDP Waste Glasses," Mater. Res. Soc. Symp. Proc. 412, 205-211 (1996).

4. G. D. Maupin, W. M. Bowen, and J. L. Daniel, *Fabrication and Characterization of MCC Approved Testing Material– ATM-10 Glass*, Pacific Northwest Laboratory Report PNL-5577-10 (1988).

5. W. L. Ebert, "Laboratory Testing of West Valley Reference 6 Glass," Ceram. Trans. 61, 471-478 (1995).

6. D. McPherson, I. Joseph, A. Mathur, C. Capozzi, S. Armstrong, and L. D. Pye, *The Influence of Waste Variability on the Properties and Phase Stability of the West Valley Reference Glass*, West Valley Nuclear Services Co., Inc. Report DOE/NE/44139-29 (1987).

7. J. K. Bates and T. J. Gerding, *NNWSI Phase II Materials Interaction Test Procedure and Preliminary Results*, Argonne National Laboratory Report ANL-84-81 (1984).

8. J. K. Bates and T. J. Gerding, *One-Year Results of the NNWSI Unsaturated Test Procedure: SRL 165 Glass Application*, Argonne National Laboratory Report ANL-85-41 (1986).

9. A. B. Woodland, J. K. Bates, and T. J. Gerding, *Parametric Effects on Glass Reaction in the Unsaturated Test Method*, Argonne National Laboratory Report ANL-91/36 (1990).

10. Site Characterization Plan, U.S. Department of Energy, Office of Civilian Radioactive Waste Management, DOE Report DOE/RW-0199 (1988).

11. T. A. Abrajano, J. K. Bates, A. B. Woodland, J. P. Bradley, and W. L. Bourcier, "Secondary Phase Formation during Nuclear Waste Glass Dissolution," Clays and Clay Minerals 38(5), 537-538 (1990).

12. G. L. Kehl, *The Principles of Metallographic Laboratory Practice*, McGraw-Hill, NY, pp. 61-79 (1949).

13. J. K. Bates, J. P. Bradley, A. Teetsov, C. R. Bradley, and M. Buchholtz ten Brink, "Colloid Formation during Waste Form Reaction: Implications for Nuclear Waste Disposal," Science 256, 649-651 (1992).

14. J. A. Fortner, T. J. Gerding and J. K. Bates, "Long-Term Test Results from a West Valley Actinide-Doped Reference Glass," Ceram. Trans. 61, 455-462 (1995).

15. J. K. Bates, C. R. Bradley, E. C. Buck, J. C. Cunnane, W. L. Ebert, X. Feng, J. J. Mazer, D. J. Wronkiewicz, J. Sproull, W. L. Bourcier, B. P. McGrail and M. K. Altenhoffen, *High-Level Waste Borosilicate Glass: A Compendium of Corrosion Characteristics*, J. C. Cunnane, ed., U.S. Department of Energy Report DOE-EM-0177 (1994).

16. N. Güven, "Smectites," in *Hydrous Phyllosilicates (Exclusive of Micas), Reviews in Mineralogy*, Volume 19, S. W. Bailey, ed., pp. 497-560, Mineralogical Society of America, Washington, DC (1988).

17. JCPDS, Mineral Powder Diffraction File, P. Bayliss, L. G. Berry, M. E. Mrose, A. P. Sabina, and D. K. Smith, eds., JCPDS, Swarthmore, PA (1983).

18. G. J. McCarthy, W. B. White, and D. Pfoertsch, "Synthesis of Nuclear Waste Monazites, Ideal Actinide Hosts for Geologic Disposal," Mat. Res. Bull. 13, 1239 (1978).

19. F. G. Fisher and R. Meyrowitz, "Brockite, a New Calcium Thorium Phosphate from the Wet Mountains, Colorado," Amer. Mineral. 47, 1346-1355 (1962).

20. T. Manoubi, C. Colliex, and P. Rez, "Quantitative Electron Energy Loss Spectroscopy on $M_{4,5}$ Edges in Rare Earth Oxides," J. Elect. Spec. and Related Phen. 50, 1-18 (1990).

21. J. A. Fortner and E. C. Buck, "The Chemistry of the Light Rare-Earth Elements as Determined by Electron Energy Loss Spectroscopy," Appl. Phys. Lett. (in press).

22. J. Bowles et al., "A Re-Examination of Cheralite," Mineral. Mag. 43, 885-888 (1980).

23. R. Ruh and A. Wadsley, "The Crystal Structure of $ThTi_2O_6$ (Brannerite)," Acta Crystallogr. 21, 974 (1966).

24. H. W. Jaffe, H. T. Evans, and R. W. Chapman, "Occurrence and Age of Chevkinite from the Devil's Slide Fayalite-Quartz Syenite Near Stark, New Hampshire," Amer. Mineral. 41, 474 (1956).

25. N. E. Cusak, *The Physics of Structurally Disordered Matter*, Adam Hilger, Bristol, UK, and Philadelphia, PA (1987).

26. A. J. G. Ellison, J. J. Mazer and W. L. Ebert, *Effect Of Glass Composition On Waste Form Durability : A Critical Review*, Argonne National Laboratory Report ANL-94/28 (1995).

27. J. K. Bates, A. J. G. Ellison, J. W. Emery, and J. C. Hoh, "Glass as a Waste Form for the Immobilization of Plutonium," Mater. Res. Soc. Symp. Proc. 412, 57-64 (1996).

28. R. H. Doremus, "Interdiffusion of Alkali and Hydronium Ions in Glass: Partial Ionization," J. Non-Cryst. Sol. 48, 431-436 (1982).

29. N. Pandya, D. W. Muenow, S. K. Sharma, and B. L. Sherriff, "The Speciation of Water in Hydrated Alkali Silicate Glasses," J. Non-Cryst. Solids 176, 140-146 (1994).

30. L. R. Pederson, D. R. Baer, G. L. McVay, and M. H. Engelhard, "Reaction of Silicate Glasses in D- and ^{18}O-Labelled Water," Phys. Chem. Glasses 31(5), 177-182 (1990).

31. D. R. Baer, L. R. Pederson, and G. L. McVay, "Glass Reactivity in Aqueous Solutions," J. Vac. Sci Technol. A2(2), 738-743 (1984).

32. T. A. Abrajano, J. K. Bates, and J. J. Mazer, "Aqueous Corrosion of Natural and Nuclear Waste Glasses: II. Mechanisms of Vapor Hydration of Nuclear Waste Glasses," J. Non-Cryst. Sol. 108, 269-288 (1989).

33. F. D. Ingram and M. J. Ingram, "Cell Volume Regulation Studies with the Electron Microprobe,". in *The Science of Biological Specimen Preparation for Microscopy and Microanalysis* , J.-P. Revel, T. Barnard, and G. H. Haggis, eds., pp. 139-146, SEM Inc., Chicago, IL (1986).

34. J. C. Phillips, "Topology of Covalent Non-Crystalline Solids I: Short-Range Order in Chalcogenide Alloys," J. Non-Cryst. Solids 34, 153 (1979).

35. W. L. Gong, R. C. Ewing, L. M. Wang, E. Vernaz, J. K. Bates, and W. L. Ebert, "Secondary Phase Formation and the Microstructural Evolution of Surface Layers During Vapor Phase Alteration of the French SON68 Nuclear Waste Glass at 200°C," Mater. Res. Soc. Symp. Proc. 412, 197-204 (1996).

36. Y. Inagaki, A. Ogata, H. Furuya, K. Idemitsu, T. Banba, and T. Maeda, "Effects of Redox Condition on Waste Glass Corrosion in the Presence of Magnetite," Mater. Res. Soc. Symp. Proc. 412, 257-264 (1996).

Distribution for ANL-96/16

Internal:

A. J. Bakel
J. K. Bates (20)
E. C. Buck
J. C. Cunnane
N. L. Dietz
T. DiSanto
W. L. Ebert
J. W. Emery
P. A. Finn
J. Fortner
L. D. Hafenrichter
J. E. Harmon
J. C. Hoh
T. R. Johnson
J. J. Laidler
J. S. Luo
C. J. Mertz
L. Nuñez
R. T. Riel
M. J. Steindler
D. M. Strachan
M. T. Surchik
C. E. Till
S. Vogler
S. F. Wolf
D. J. Wronkiewicz
TIS Files

External:

DOE-OSTI (2)
ANL-E Library
ANL-W Library
Manager, Chicago Operations Office, DOE
A. Bindokas, DOE-CH
J. Haugen, DOE-CH
Chemical Technology Division Review Committee Members:
- H. U. Anderson, University of Missouri-Rolla, Rolla, MO
- E. R. Beaver, Monsanto Company, St. Louis, MO
- D. L. Douglas, Consultant, Bloomington, MN
- R. K. Genung, Oak Ridge National Laboratory, Oak Ridge, TN
- J. G. Kay, Drexel University, Philadelphia, PA
- R. A. Osteryoung, North Carolina State University, Raleigh, NC
- G. R. St. Pierre, Ohio State University, Columbus, OH

J. Allison, Westinghouse Savannah River Company, Aiken, SC
N. E. Bibler, Westinghouse Savannah River Company, Aiken, SC
W. Bourcier, Lawrence Livermore National Laboratory, Livermore, CA
K. A. Chacey, USDOE, Office of Environmental Management, Germantown, MD
M. O. Cloninger, Mac Technical Services, Inc., Richland, WA
S. P. Cowan, USDOE, Office of Waste Management, Germantown, MD
P. Dirkmaat, USDOE, Idaho Operations Office, Idaho Falls, ID
R. S. Dyer, Yucca Mountain Project Office, Las Vegas, NV
R. E. Erickson, USDOE, Office of Environmental Management, Germantown, MD
R. C. Ewing, University of New Mexico, Albuquerque, NM
R. Fish, B&W Fuel Company, Las Vegas, NV
C. W. Frank, USDOE, Office of Science and Technology, Washington, DC
T. J. Gerding, Plainfield, IL
C. Interrante, U. S. Nuclear Regulatory Commission, Washington, DC
V. J. Jain, West Valley Nuclear Services, West Valley, NY

C. Jantzen, Westinghouse Savannah River Company, Aiken, SC
L. J. Jardine, Lawrence Livermore National Laboratory, Livermore, CA
W. S. Ketola, USDOE, West Valley Project Office, West Valley, NY
D. A. Knecht, Lockheed Idaho Technology Company, Idaho Falls, ID
J. Kolts, USDOE, Idaho Operations Office, Idaho Falls, ID
J. H. Lee, Intera, Las Vegas, NV
H. H. Loo, Lockheed Idaho Technology Company, Idaho Falls, ID
W. Lutze, University of New Mexico, Albuquerque, NM
J. M. Matuszek, JMM Consulting, Del Mar, NY
P. K. Nair, Southwest Research Institute, San Antonio, TX
R. Palmer, West Valley Nuclear Services, West Valley, NY
E. C. Pearcy, Southwest Research Institute, San Antonio, TX
W. G. Ramsey, Westinghouse Savannah River Company, Aiken, SC
R. Ramsey, USDOE, Office of Environmental Management, Washington, DC
C. G. Russomanno, USDOE, Office of Civilian Radioactive Waste Management, Washington, DC
A. Simmons, USDOE, Las Vegas, NV
J. Sproull, Westinghouse Savannah River Company, Aiken, SC
D. Stahl, M&O/B&W Fuel Company, Las Vegas, NV
R. B. Stout, Lawrence Livermore National Laboratory, Livermore, CA
M. Tomozawa, Rensselaer Polytechnic Institute, Troy, NY
J. C. Tseng, USDOE, Office of Environmental Management, Germantown, MD
T. Wichmann, USDOE, Idaho Operations Office, Idaho Falls, ID
B. Grambow, Kernforschungszentrum Karlsruhe, GERMANY
L. Johnson, Atomic Energy of Canada, Ltd., Pinawa, Manitoba, CANADA
J. Kim, Kernforschungszentrum Karlsruhe, GERMANY
P. Van Iseghem, Boeretang, BELGIUM
E. Vernaz, Centre d'Etudes Nucleares de la Valle du Rhone, Marcoule, FRANCE
L. Werme, Svensk Karnbranslehantering AB, Stockholm, SWEDEN